Cell Reports
Medicine

Article

Functional diagnostics using fresh uncultured lung tumor cells to guide personalized treatments

Graphical abstract

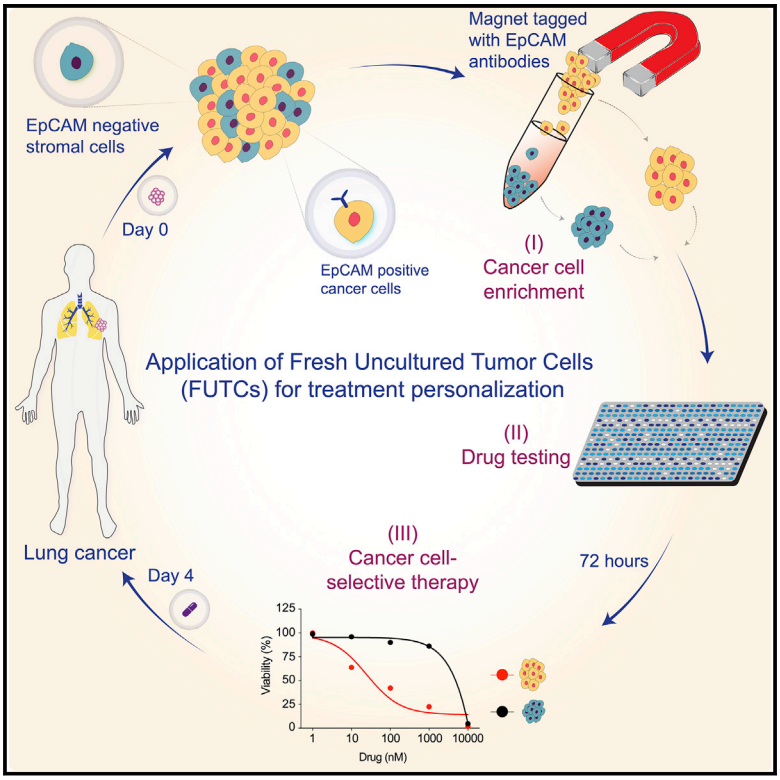

Highlights

- Fresh uncultured tumor-derived epithelial cells (FUTCs) are amenable for drug testing
- Profiling of lung tumor and matched normal cells identifies cancer-selective treatments
- NSCLC FUTCs with targetable drivers expose genotype-matched responses or non-responses
- The FUTC approach can guide personalized therapy in compassionate patient care

Authors

Sarang S. Talwelkar, Mikko I. Mäyränpää, Lars Søraas, ..., Aija Knuuttila, Krister Wennerberg, Emmy W. Verschuren

Correspondence

krister.wennerberg@bric.ku.dk (K.W.), emmy.verschuren@helsinki.fi (E.W.V.)

In brief

Point-of-care functional diagnostic tests are unavailable for lung cancer. Talwelkar et al. present a pharmacological assay that uses fresh uncultured tumor cells (FUTCs) to guide personalized therapy for lung cancer patients. Besides identifying genotype-matched drug sensitivities, FUTC profiling also predicts clinical non-responses and can be used to expose resistance mechanisms.

Talwelkar et al., 2021, Cell Reports Medicine 2, 100373
August 17, 2021
https://doi.org/10.1016/j.xcrm.2021.100373

CellPress

Cell Reports Medicine

CellPress
OPEN ACCESS

Article

Functional diagnostics using fresh uncultured lung tumor cells to guide personalized treatments

Sarang S. Talwelkar,[1] Mikko I. Mäyränpää,[2,3] Lars Søraas,[4] Swapnil Potdar,[1] Jie Bao,[1] Annabrita Hemmes,[1] Nora Linnavirta,[1] Jon Lømo,[5] Jari Räsänen,[6] Aija Knuuttila,[7] Krister Wennerberg,[1,8,*] and Emmy W. Verschuren[1,9,*]

[1]Institute for Molecular Medicine Finland (FIMM), HiLIFE, University of Helsinki, Helsinki 00014, Finland
[2]HUSLAB, Division of Pathology, Helsinki University Hospital and University of Helsinki, Helsinki 00029, Finland
[3]Department of Pathology, University of Helsinki, Helsinki 00014, Finland
[4]Pontoppidans Gate 9B, 0462 Oslo, Norway
[5]Department of Pathology, Oslo University Hospital, Oslo, Norway
[6]Department of Thoracic Surgery, Heart and Lung Center, Helsinki University Hospital, Helsinki, Finland
[7]Department of Pulmonary Medicine, Heart and Lung Center, and Cancer Center, Helsinki University Hospital, Helsinki, Finland
[8]BRIC-Biotech Research & Innovation Centre and Novo Nordisk Foundation Center for Stem Cell Biology (DanStem), University of Copenhagen, 2200 Copenhagen, Denmark
[9]Lead contact
*Correspondence: krister.wennerberg@bric.ku.dk (K.W.), emmy.verschuren@helsinki.fi (E.W.V.)
https://doi.org/10.1016/j.xcrm.2021.100373

SUMMARY

Functional profiling of a cancer patient's tumor cells holds potential to tailor personalized cancer treatment. Here, we report the utility of fresh uncultured tumor-derived EpCAM$^+$ epithelial cells (FUTCs) for *ex vivo* drug-response interrogation. Analysis of murine *Kras* mutant FUTCs demonstrates pharmacological and adaptive signaling profiles comparable to subtype-matched cultured cells. By applying FUTC profiling on non-small-cell lung cancer patient samples, we report robust drug-response data in 19 of 20 cases, with cells exhibiting targeted drug sensitivities corresponding to their oncogenic drivers. In one of these cases, an *EGFR* mutant lung adenocarcinoma patient refractory to osimertinib, FUTC profiling is used to guide compassionate treatment. FUTC profiling identifies selective sensitivity to disulfiram and the combination of carboplatin plus etoposide, and the patient receives substantial clinical benefit from treatment with these agents. We conclude that FUTC profiling provides a robust, rapid, and actionable assessment of personalized cancer treatment options.

INTRODUCTION

The concept of precision medicine means giving the right drug to the right individual at the right time. In this context, genotype-guided pairing of tumors with drugs that target tumor-selective driver mutations has been in clinical practice for >2 decades. For non-small-cell lung cancer (NSCLC) patients, inhibitors targeting EGFR, KRAS (G12C), ALK, BRAF, MET, and ROS are approved for genotype-guided indications that match for ~40% of patients.[1] However, even with the genetic matches, only 50%–70% of treated patients benefit from these treatments. When attempting to use genotype-guided therapies beyond currently approved indications, trials have shown that only 10% of patients can be paired with genomics-matched targeted treatments, and at best one-third of these receives clinical benefit.[2,3] Hence, the prediction of successful precision anticancer treatments at the individual level remains challenging, largely because of extensive genomic and phenotypic heterogeneity of many cancer types, including NSCLC. Therefore, to identify precision medicines for the majority of NSCLC patients, we need additional tools beyond those that are currently used in the clinic.

Combining static genetic measurements with pharmacological interrogation of patient-derived cancer cells can provide a more comprehensive approach for predicting effective treatments[4–6]; however, proof of its clinical utility is lacking, particularly for solid tumors. For patients with hematological malignancies, we and others have successfully implemented individualized treatment strategies guided by *ex vivo* drug-response testing of patient biopsies.[7,8] Based on these early successes of *ex vivo* testing to tailor patient treatments, multiple clinical trials were initiated for leukemia patients (e.g., NCT01620216, NCT04267081). For solid tumors, similar functional diagnostic methodologies can, however, not readily be adopted; the reasons include the fragile and short-lived nature of tissues (e.g., those observed in organotypic tumor slice cultures[9,10]) and a general lack of robust methods to isolate and propagate primary epithelial cells.

In promising recent developments, new culture and organoid approaches enabling the long-term expansion of primary epithelial cells have been introduced.[4,11,12] Toward translational applications, the use of conditionally reprogrammed (CR) cultures derived from clinical lung tumors successfully identified novel

actionable treatments and molecular mechanisms underlying drug resistance.[4,13,14] Similarly, NSCLC organoids have been shown to recapitulate oncogenic addictions and the tissue architecture of the original tumors, offering an optional model for exploring inter- and intratumoral functional heterogeneity.[15,16]

While the implementation of CR or organoid cultures in principle permits drug-response profiling of patient-derived cells, these models take a long time to be established, and, more important, do not guarantee the expansion of malignant cells.[4,15,17] Their functional interrogation will therefore unlikely lead to significant effects on personalized diagnostics and patient care.[11] To circumvent the challenges associated with *ex vivo* cultures, we tested the utility of fresh uncultured tumor-derived cells (FUTCs) for drug-response assessment. Using this approach, we present a diagnostic assay for the rapid identification of actionable treatments using patient-derived tumor cells.

RESULTS

Tumor-derived epithelial cultures often do not represent malignant cells

With the aim of identifying individualized treatment options, and to understand genetic driver-drug-response relationships, we established NSCLC patient-derived primary cultures to allow for pharmacogenomic screening. Patient-derived primary cultures were established using CR methodology, which allows *ex vivo* establishment and indefinite propagation of epithelial cells from both normal and malignant specimens.[18] To confirm the identity of the tumor-derived cultures, we performed targeted next-generation sequencing for 578 cancer-related genes in 11 primary cultures, as well as matched tumor and adjacent normal lung tissues. Altogether, 71 nonsynonymous somatic mutations in 47 genes were detected in tumor tissues (Table 1). Of the 11 tested cultures, 9 lacked the oncogenic mutations detected in the reference tumor. Notably, the two cultures that showed a concordance of mutations with their respective source tissue were derived from different regions from the same tumor (Table 1). The success rate of establishing patient-derived malignant cultures was therefore limited to ~10%. In accordance with previous findings,[17,19,20] our results argue that CR culture establishment is not an effective approach for the generation of pharmacogenomic screening data from NSCLC patient samples.

Murine FUTCs capture drug responses of other *ex vivo* cell culture systems

To address the challenge of cell culture adaptation, we investigated whether freshly isolated epithelial cell adhesion molecule (EpCAM)-expressing epithelial cells can directly be used for drug-response assessment. We performed functional profiling of FUTCs and CR cultures derived from murine NSCLC tumors obtained from $Kras^{G12D};Lkb1^{fl/fl}$ (KL) and $Kras^{G12D};p53^{fl/fl}$ (KP) models. These models were selected because (1) they represent tumors with common genetic drivers and histopathological diversities detected in clinical specimens,[21] (2) they allow CR culture establishment with relative ease, permitting comparisons of tumor-matched FUTCs and cultures (Figure 1A), and (3) we have gained understanding on their tumor subtype-selective drug sensitivities.[22]

First, we confirmed that FUTCs survive and grow during culture by measuring cellular ATP levels using CellTiter-Glo (CTG). FUTCs from the different tumor groups exhibited significantly higher CTG readouts after 3 days of culture (Figure 1B). Second, we assessed the utility of FUTCs to predict known genotype-selective drug sensitivities. We confirmed that only p53-expressing FUTCs responded to the Mdm2-p53 interaction inhibitor idasanutlin (Figures 1C and 1F). Moreover, KL-derived FUTCs exhibited selective responses to HSP90 inhibition (Figures 1D and 1F), corroborating findings from cultured lung cancer models.[22–24] Lastly, we confirmed that gemcitabine, an approved chemotherapeutic agent for NSCLC treatment, potently inhibited the viability of both KL and KP cells (Figures 1E and 1F), matching previous findings in CR cultures.[22] In further agreement with published data,[25,26] a synergistic interaction was detected between MEK and ERBB receptor family inhibition in KL, but not in KP FUTCs (Figure 2A). We also could confirm adaptive reactivation of the mitogen-activated protein kinase (MAPK) and phosphatidylinositol 3-kinase (PI3K) signaling pathways, detected by the re-phosphorylation of ERK and AKT after extended MEK inhibition, described in many other NSCLC studies, including our murine CR cultures (Figures 2B–2D and S1).

Patient-derived FUTCs are amenable for pharmacological profiling

To test a FUTC-based approach with patient-derived cells, we conducted a drug sensitivity and resistance testing (DSRT) study on 19 clinical NSCLC samples (Table S1). Tumor tissue analysis by immunohistochemistry (IHC) revealed inter- and intratumor heterogeneity for EpCAM expression levels, 13 of 19 tumor samples (68%) showed high EpCAM expression, while 11% and 21% samples showed moderate and low EpCAM expression, respectively (Table S2). To identify drug responses selective to tumor-derived $EpCAM^+$ cells, responses were compared to tumor-derived non-epithelial $EpCAM^-$ cells, and also to healthy lung tissue-derived $EpCAM^+$ cells as tissue-matched controls (Figure 3A). Similar to the murine FUTCs, the patient-derived FUTCs exhibited good viability in culture (Figures 3B, S2A, and S2B). Furthermore, analysis of *KRAS* mutations in 6 patient samples revealed an average 3.7-fold enrichment of cancer cells in tumor-derived $EpCAM^+$ cell fractions compared to matched bulk tumor tissues (Figures 3C and S2C). Similarly, $EpCAM^+$ fractions derived from samples carrying an ALK rearrangement exhibited enrichment of *ALK* fusion-carrying cells (Figure S2D).

Next, we performed screening with 66 lung cancer-selective drugs on 14 samples, or with smaller compound sets on 5 samples in which only limited $EpCAM^+$ FUTCs could be isolated, and for 18/19 samples, we observed robust drug screening data ($Z' > 0.2$). Unsupervised hierarchical clustering of the drug sensitivity scores revealed that technical replicates from the same patient sample cluster together, thus confirming robustness of the screening data generated using FUTCs (Figures 3D and 3E). Through multifactorial analyses, we showed that the robustness of the screening data correlated with the cancer cell fraction in the tumor tissue (Figures 3F and S2E). Moreover, samples with higher percentages of $Ki\text{-}67^+$ cancer cells exhibited higher CTG activities *ex vivo* (Figures 3G and S2E). These results

Table 1. Genomic analysis of NSCLC tumor tissue and tumor-derived CR cultures

Sample no.	Sample ID	Gender/age	Tumor type	Tumor tissue (variant allele frequency)	Tumor-derived CR culture[a] (variant allele frequency)
1	PLT26; region-3	F/55	AC	TFG (0.10), CBFA2T3 (0.10), SMARCA4 (0.08), TP53 (0.07), TMPRSS2 (0.07), PPP2R1A (0.04), ALK$^+$	TFG (0.66), CBFA2T3 (0.73), SMARCA4 (0.45), TP53 (0.99), TMPRSS2 (0.54), PPP2R1A (0.50), ALK$^+$
2	PLT26; region-5	F/55	AC	TFG (0.15), CBFA2T3 (0.28), SMARCA4 (0.15), TP53 (0.28), TMPRSS2 (0.17), PPP2R1A (0.12), ALK$^+$	TFG (0.64), CBFA2T3 (0.66), SMARCA4 (0.49), TP53 (0.98), TMPRSS2 (0.50), PPP2R1A (0.58), ALK$^+$
3	PLT30	M/75	AC	NKX2-1 (0.33), ERB B4 (0.26), WASF 3 (0.25), KRAS (0.18), TP53 (0.15), HERPUD1 (0.14)	All wild type
4	PLT36	F/62	AC	GNAS (0.72), TP53 (0.40), LTBP2 (0.34), LCP1 (0.3), MAP2K1 (0.27), PDGFRB (0.25), GUCY1A2 (0.19), KMT2D (0.16), HECW1 (0.15), KMT2C (0.10)	All wild type
5	PLT41	M/56	AC	MYB (0.15), NSD3 (0.14), TP53 (0.14), KMT2C (0.11), ALK$^+$	All wild type
6	PLT42[b]	F/63	AC	PDGFRB (0.05), TYK2 (0.04), ARID1A (0.03), IDH2 (0.03), TCL6 (0.03), ITK (0.03), NTRK3 (0.02), KRAS (0.02), WT1 (0.02)	All wild type
7	PLT62; region-1	F/50	AC	BCL6 (0.66), STK11 (0.43), KRAS (0.38), PRF1 (0.33), KIT (0.22), NEF 2L2 (0.20), CBFA2T3 (0.19), CLTCL1 (0.17)	All wild type
8	PLT62; region-2	F/50	AC	BCL6 (0.34), STK11 (0.26), KRAS (0.23), PRF1 (0.17), KIT (0.10), NEF2L2 (0.04), CBFA2T3 (0.07), CLTCL1 (0.10)	All wild type
9	PLT63	F/68	AC	CDKN2B (0.11), ALK$^+$	All wild type
10	PLT64	F/25	AC	ALK$^+$	All wild type
11	PLT66	M/71	AC	CIC (0.42), KRAS (0.36), CBF A2T3 (0.23), AKAP9 (0.22), NIN (0.22), AFF4 (0.21), PML (0.20), FGFR1OP (0.20), ABL1 (0.19), FLT3 (0.19), LTBP2 (0.19), PDGFRB (0.18), HEY1 (0.18), EPHA10 (0.17), UNC13D (0.16), CDH6 (0.16), ARID4B (0.14), BCL11B (0.14), UNC13D (0.11), CYP1B1 (0.10)	All wild type

[a]Passage #4.
[b]All mutations identified with variant allele frequency <0.1.

indicate that FUTCs are relevant *ex vivo* models of tumor tissue and that this single-cell population can be diagnostically profiled before culture establishment.

Responses to approved targeted therapies are exposed with patient-derived FUTCs

To further validate the diagnostic use of the FUTC assay, responses to well-established targeted receptor tyrosine kinase inhibitors were analyzed. Tumor-derived EpCAM$^+$, but not EpCAM$^-$, cells from 4 *EGFR* mutant patient samples (L858R and E746-A750del) responded to several classes of EGFR inhibitors. Third-generation mutant-selective osimertinib selectively and most effectively reduced the viability of *EGFR* mutant EpCAM$^+$ tumor cells (drug sensitivity score [DSS] > 10), while the second-generation pan-ERBB inhibitor afatinib (AF) reduced the viability of both tumor and normal EpCAM$^+$ cells (Figures 4A and 4B). These results are consistent with the known superior selectivity of osimertinib toward mutant *EGFR*.[27–30] Similarly, in FUTCs derived from a clinical sample carrying an activating exon 14 skipping mutation in the *MET* gene, the ALK/MET

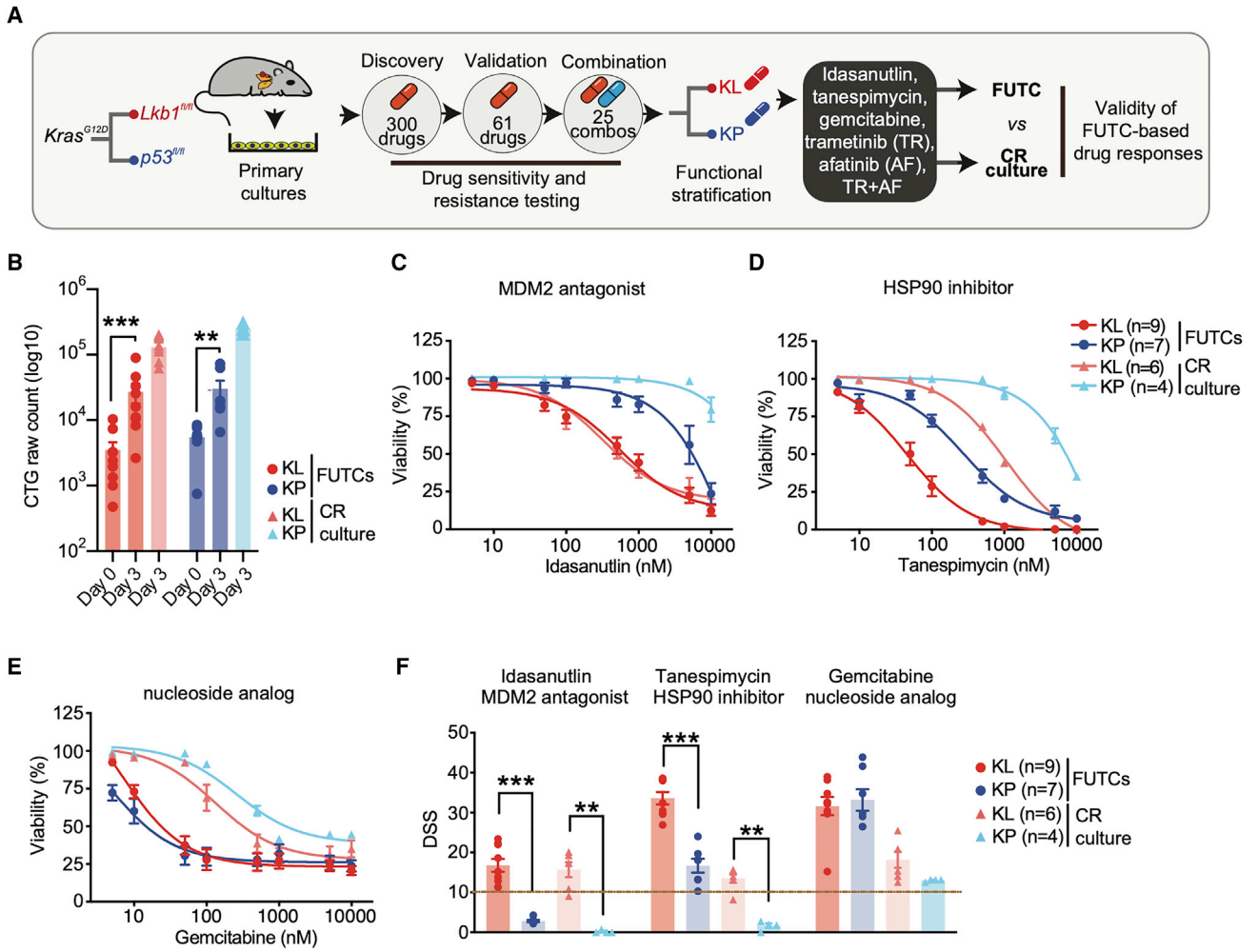

Figure 1. Murine FUTCs exhibit functional profiles comparable to conditionally reprogrammed cultures

(A) Schematic of comprehensive drug testing of KP and KL tumor-derived cultures to validate the ability of FUTCs to identify subtype-selective treatments.

(B) Viability assessment of FUTCs at 0 and 72 h.

(C–E) Dose-response curves of tumor-matched FUTCs and CR cultures treated for 72 h with (C) idasanutlin (MDM2 antagonist), or (D) tanespimycin (HSP90 inhibitor), or (E) gemcitabine (nucleoside analog).

(F) DSS calculated for (C)–(E) and compared between KL and KP subtypes for both FUTCs and CR cultures.

Data are represented as means ± SEMs. Student's t test: *p < 0.05, **p < 0.01, ***p < 0.001.

inhibitor crizotinib showed the strongest sensitivity (DSS > 10), and this was selective for EpCAM$^+$ tumor cells (Figures 4C and 4D). Importantly, genotype-matched sensitivities were only observed in EpCAM$^+$ cells, not in bulk tumor-derived cell populations, indicating that EpCAM enrichment is required for identification of cancer-specific vulnerabilities (Figures S3A and S3B).

Contrasting with the above target-matched responses, EpCAM$^+$ cells derived from three ALK fusion$^+$ tumors showed low sensitivity to the ALK inhibitors ceritinib and crizotinib (Figures 4E and 4F). Since the epithelial-to-mesenchymal transition (EMT) can explain resistance to ALK inhibitors,[31,32] primary tumor tissues were stained with epithelial E-cadherin and mesenchymal vimentin markers (Table S2; 6 of 18 patient samples showed vimentin staining-positive tumor cells). This confirmed EMT in all three ALK$^+$ samples tested in the FUTC assay (Figures 4G and S2E), possibly explaining why these samples demonstrated a poor response to ALK inhibition. Thus, FUTC-based profiling can gauge targeted kinase inhibitor responses and non-responses in patient samples that carry the respective driver mutations.

Pharmacological profiling of *KRAS* mutant patient-derived FUTCs demonstrates inter- and intratumoral heterogeneity

We next asked how FUTC-based profiling captures sample-selective functional heterogeneity in *KRAS* mutant samples, which overall represent 25%–30% of NSCLC, yet stratify further due to differences in, among others, histopathology, metabolism, or co-occurring mutations. Comparison of drug responses of 7 *KRAS* mutant and 11 *KRAS* wild-type samples identified the MEK

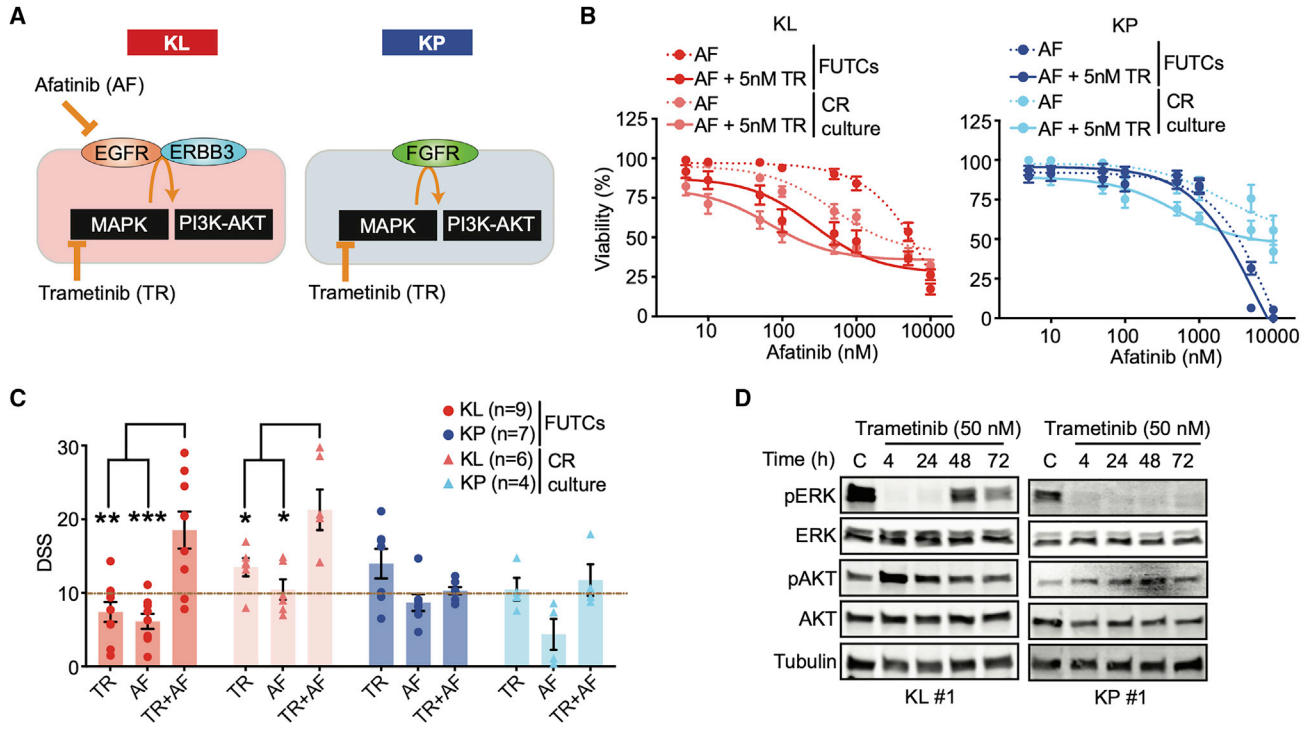

Figure 2. Murine FUTCs show treatment-adaptive signaling mechanisms

(A) Graphic model for subtype-selective adaptive activation of MAPK and PI3K-AKT pathways in murine *Kras* mutant NSCLC cultures.

(B) Dose-response curves of FUTCs and CR cultures treated trametinib (TR), afatinib (AF), and combination treatment. For the combination screen, 5 nM TR was used together with a dose series of AF.

(C) DSS calculated for (B) and compared between KL and KP subtypes for both FUTCs and CR cultures.

(D) Immunoblots of KL and KP FUTCs treated with vehicle (C; DMSO) and or treated with 50 nM TR for various time points (4, 24, 48, and 72 h), and probed with indicated antibodies.

Error bars represent ±SEMs. Student's t test: *p < 0.05, **p < 0.01, ***p < 0.001.

inhibitor trametinib (TR) as the most *KRAS* mutant-selective compound, but also other MAPK inhibitors showed KRAS-selective responses, albeit with a less stringent statistical difference (Figure 5A; Table S3). This aligned with the analysis of lung cancer cell lines in the Genomics of Drug Sensitivity in Cancer (GDSC) database,[33] revealing MAPK inhibitors as the most *KRAS* mutant selective (Figure S3A). Moreover, TR selectively inhibited *KRAS* mutant cells without affecting tumor-derived EpCAM$^-$ and normal tissue-derived EpCAM$^+$ control cells (Figure 5B). Correlation analysis of the drug sensitivities of individual *KRAS* mutant samples to average drug sensitivities of *KRAS* wild-type samples indicated intertumoral heterogeneity; each *KRAS* mutant sample exhibited a unique drug-response profile, and even for shared hits such as TR, the actual efficacies varied between samples. As anticipated, of a total of 27 hits, 14 compounds selective for *KRAS* mutant FUTCs either targeted the MAPK or the PI3K-AKT pathways (Figures 5C and S3B).

To assess intratumoral functional heterogeneity, drug responses in FUTCs derived from two different regions from the same patient sample (PLT62) were compared. Both tumor regions carried identical genetic alterations (Figure S4A), including *STK11* and *NFE2L2* mutations known to confer resistance to MEK inhibition in *KRAS* mutant lung cancer.[24,34] A combinatorial screen of 66 drugs in combination with TR showed that region-2 cells exhibited a relatively higher sensitivity to MAPK inhibitors (Figures 5D and 5E), while region-1 cells showed selective sensitivity to combinatorial treatment with TR plus PI3K-AKT pathway inhibitors (Figures 5F and 5G). Consistent with the drug sensitivity data, cancer cells from region-1 exhibited a higher percentage of pERK$^+$ and p4EBP1$^+$ cells, as well as cells dually stained for these markers, jointly indicating a potential tumor region-selective codependency on MAPK and PI3K-AKT pathways (Figures S4B and S4C). Interestingly, FUTCs from both tumor regions showed combinatorial response to TR plus the BCL-2/BCL-xL inhibitor navitoclax (NA) (Figure 5H), a combination described to convey synthetic lethality in *KRAS* mutant tumors.[35]

These data show that FUTC profiling can expose inter- and intratumoral functional heterogeneity in *KRAS* mutant NSCLC (Figures 5C–5G; Table S2), and tentatively indicates their use in identifying tissue-selective drug combinations. As in murine samples, feedback activation of the MAPK and PI3K-AKT pathways, measured by rebound ERK and AKT phosphorylation, was detected following TR treatment in KRAS mutant FUTCs from PLT87 (Figure 5I). Although analysis of more samples is warranted, these preliminary results suggests that deeper functional profiling of FUTCs may further help to identify drug combinations that target adaptive signaling mechanisms.

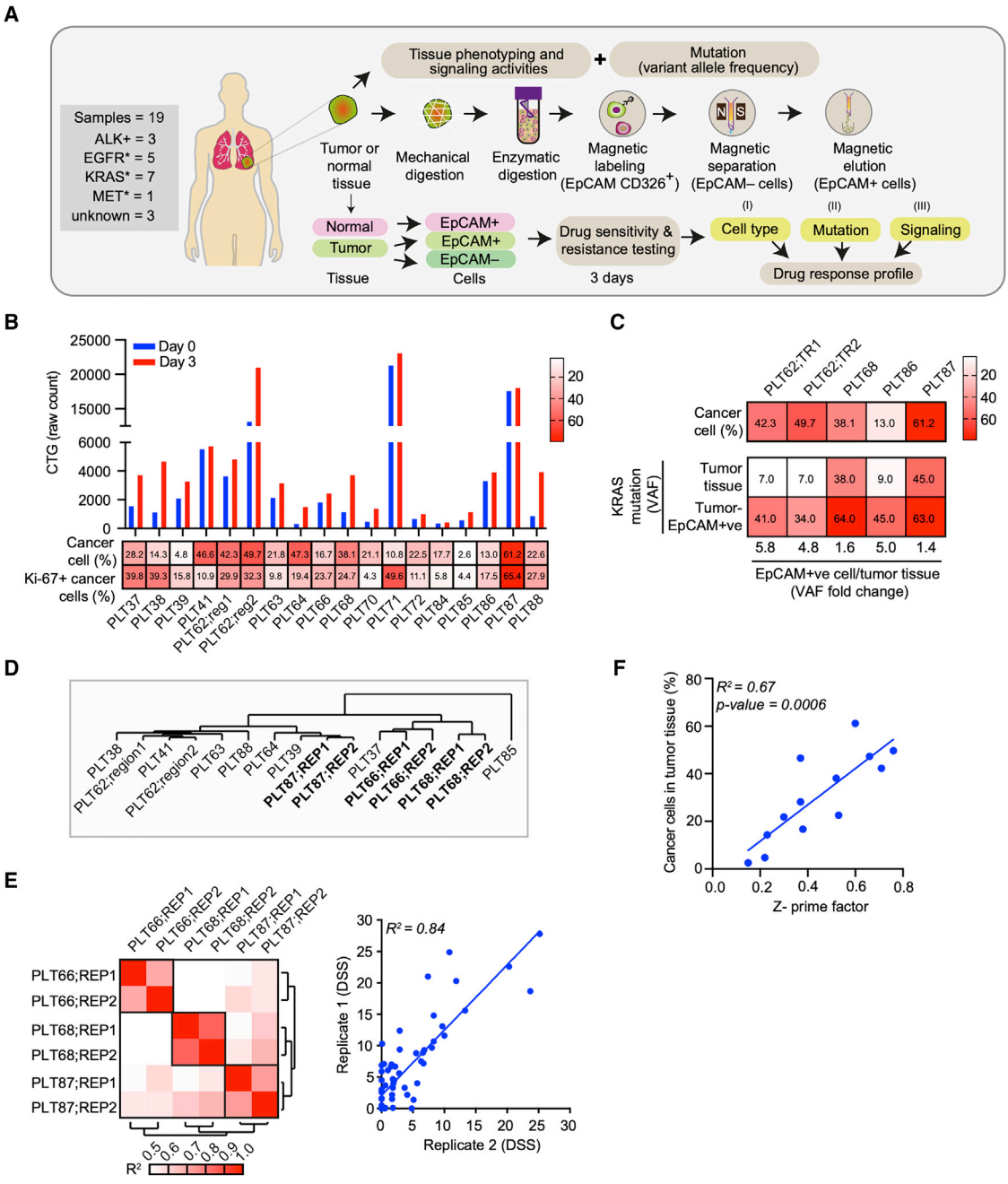

Figure 3. Application of patient-derived FUTCs for pharmacological screening

(A) Schematic of FUTC-based drug sensitivity and resistance testing from clinical specimens.

(B) Viability assessment of patient-derived cells at days 0 and 3 after seeding in 384-well plates. Heatmap showing percentages of total cancer cells and Ki-67^{+} cancer cells normalized to total cancer cells in the tumor tissue.

(C) Heatmap representing percentage of cancer cells and *KRAS* mutation variant allele frequencies in patient-matched tumor tissues versus tumor-derived EpCAM^{+} cells.

(D) DSS (66 compounds) of tumor-derived EpCAM^{+} cells were clustered by using a complete linkage method, coupled with Euclidean distance measurement.

(E) Heatmap of Pearson's correlation coefficient values between technical replicates of the same sample, or samples from different patients (left). Representative correlation plots of DSS values, comparing technical replicate screens of PLT68 (right).

(F) Correlation plot comparing the association between the percentage of cancer cells in the tumor tissue and Z′prime factors obtained from respective DSRT screens.

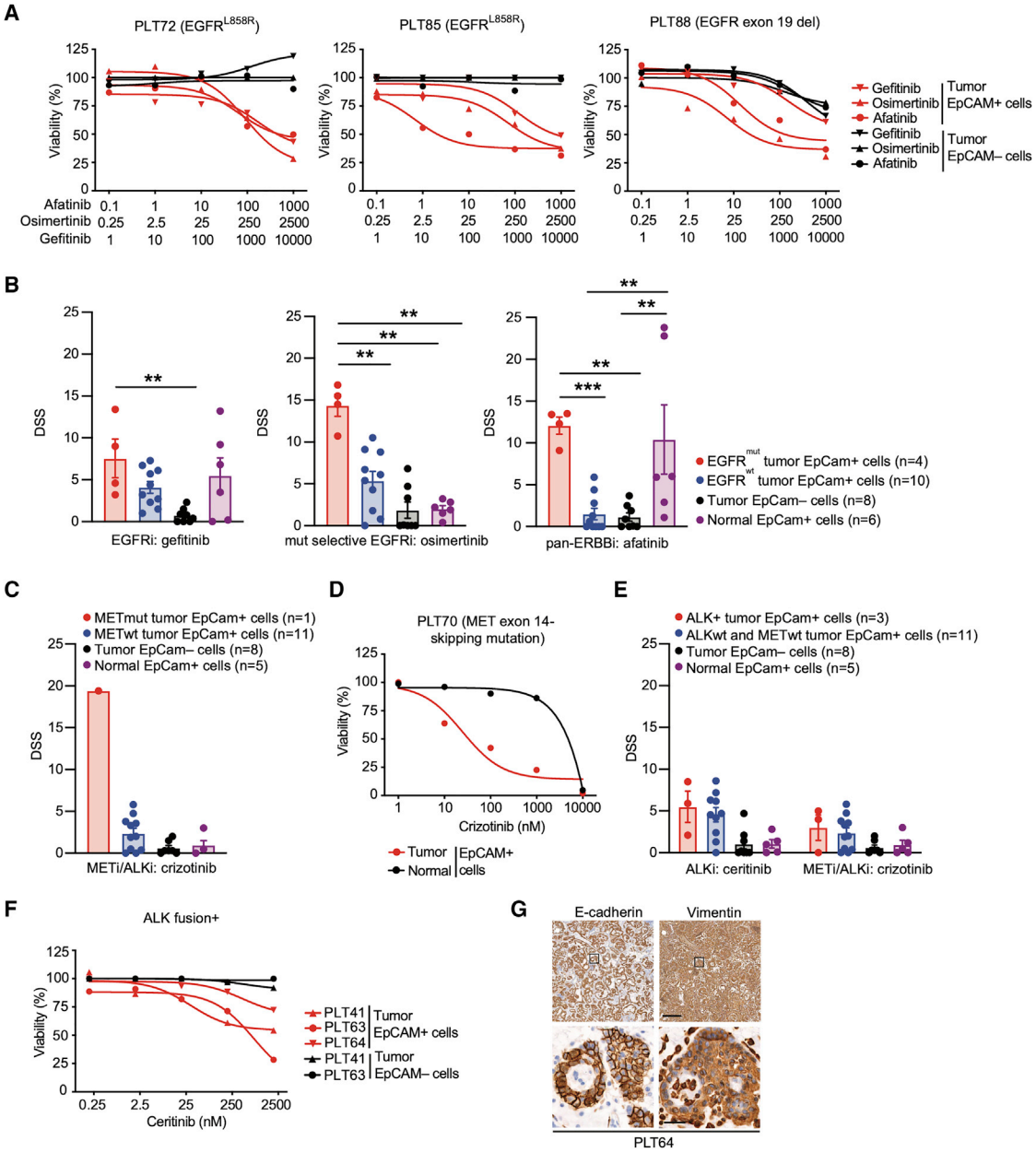

Figure 4. NSCLC FUTCs predict genotype-matched therapeutic responses

(A) Dose-response curves of gefitinib, osimertinib, and AF in patient-matched tumor-derived EpCAM$^+$ and EpCAM$^-$ cells.

(B) DSS for gefitinib, osimertinib, and AF compared between *EGFR* mutant EpCAM$^+$, *EGFR* wild-type EpCAM$^+$, tumor EpCAM$^-$, and normal EpCAM$^+$ cells. Each dot represents an independent sample.

(C and D) Bar graph representing the DSS of crizotinib (C) and (D) ceritinib and crizotinib across all of the patient samples.

(E) Dose-response curves of crizotinib in patient-matched tumor-derived EpCAM$^+$ or normal tissue-derived EpCAM$^+$ cells.

(F) Dose-response curves of ceritinib in patient-matched tumor-derived EpCAM$^+$ and EpCAM$^-$ cells.

(G) Representative IHC images of E-cadherin and vimentin staining in patient (PLT64)-derived EML4-ALK$^+$ lung tumor tissues. Scale bars correspond to 200 or 20 μm for low or high magnifications, respectively. Boxes indicate areas shown in the higher magnification in a lower row.

Error bars represent ±SEMs. Two-tailed unpaired Student's t test: *p < 0.05, **p < 0.01, ***p < 0.001.

Compassionate implementation of a FUTC-based functional diagnostic assay

Finally, we report a case in which FUTC-based drug-response assessments were used to implement compassionate treatment for a patient with refractory metastatic lung cancer. This patient had been diagnosed with *EGFR* mutant stage IV lung adenocarcinoma (AC) 3.5 years earlier and had since been treated with both erlotinib and osimertinib, yet experienced disease

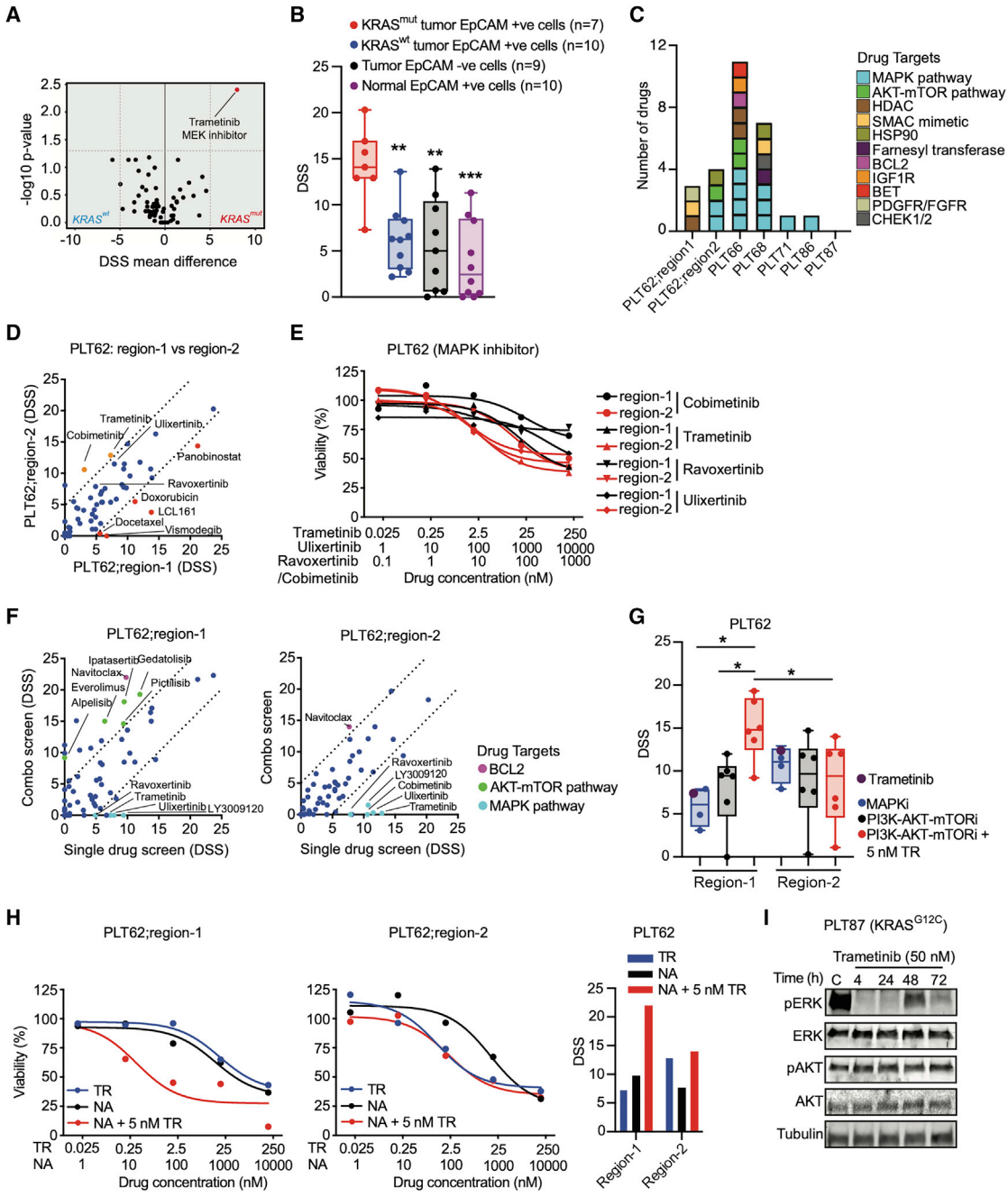

Figure 5. Functional profiling of *KRAS* mutant FUTCs reveals inter- and intratumoral heterogeneity

(A) Volcano plot displaying an association between responses to drug candidates and *KRAS* mutation status. DSS comparisons were made between *KRAS* mutant cells (n = 7) and *KRAS* wild-type cells (n = 11) for 66 oncology drugs using a 2-sided Wilcoxon signed-rank test; DSS difference >±5 and $p < 0.05$ were considered as a hit and highlighted with red color.

(B) DSS for TR compared between different cell populations; each dot represents an independent sample.

(C) The number and target of unique hits identified for an individual patient sample. Boxes are color-coded based on target, and each box represents a single drug.

(D) Correlation plots of comparing DSS obtained from FUTCs derived from different tumor regions of the same patient specimen (PLT62). Drug candidates with DSS difference >±5 are color-coded with red and orange representing region-1 and region-2 selective hits, respectively.

(E) Dose-response curves following indicated MAPK inhibitor treatments in different regions of PLT62.

(F) Correlation plots comparing DSS of 66 oncology drugs as a single agent or in combination with 5 nM TR.

(G) Dot plot displaying DSS of single treatments of MAPK inhibitors (n = 4) and PI3K-AKT-mTOR (mammalian target of rapamycin) inhibitors (n = 6) as a single agent or in combination with 5 nM TR.

(legend continued on next page)

recurrence, as evidenced by the emergence of multiple nodular lesions in the lungs and widespread metastatic lesions, concomitant with increases in the levels of carcinoembryonic antigen (CEA) and neuron-specific enolase (NSE) tumor markers. At this point, a metastatic lesion from the neck region was surgically resected, and FUTCs were used for replicate testing of 233 relevant drugs or drug combinations (Figures 6A–6C).

The drug sensitivity screen demonstrated poor response to multiple EGFR inhibitors (Figure S5A), in line with the acquired clinical resistance to erlotinib and osimertinib. To identify effective treatment options with minimal generic toxicities, we implemented a two-step process. In step 1, we identified the 20 treatments with the highest DSSs (Figure 6D). In step 2, we filtered the potent hits from step 1, based on whether the response was selective toward the patient's cancer cells over normal lung CR cells (n = 6) derived from independent patients (Figure S5B). This allowed narrowing down of the list and eliminated 15 treatments with generic toxicities. From this analysis, we identified five treatments with selective potency toward the tumor-derived cells, including disulfiram and carboplatin combined with etoposide (Figure S5C). Conversely, the FUTC-based profiling results were in agreement with the clinical non-responses to therapies targeting PI3K and ALK, even though the tumor cells harbored activating mutations in *PIK3CA* and showed overexpression of *ALK* (Figures 6G, S5D, and S5E).

Based on these results, the scheduled carboplatin plus pemetrexed, which showed inferior sensitivity compared with carboplatin plus etoposide, was changed and the patient received disulfiram and five cycles of carboplatin plus etoposide with or without disulfiram. The patient received carboplatin/etoposide/disulfiram treatment every time an increase in the CEA/NSE level was observed. This resulted in a therapeutic benefit from the FUTC-defined chemotherapy during the first 3 treatment cycles (for the total span of 7 months), as detected by a decrease in tumor size analyzed by computed tomography imaging, as well as reduced levels of CEA and NSE (Figures 6E, 6F, and S6A–S6E). Interestingly, IHC analysis of the tumor tissue done a few months following treatment onset revealed two spatially intermixed subtypes of tumor populations: (1) an SCLC population with NSE expression and (2) a squamous cell carcinoma (SCC) population with CEA expression (Figure 6G). Histological transformation to SCLC or SCC are known acquired resistance mechanisms in *EGFR* mutant AC patients treated with EGFR inhibitors,[36,37] and platinum plus etoposide is an effective treatment strategy for SCLC patients,[38,39] which the FUTC-based drug testing had identified independently of the histological analyses. However, in line with the poor prognosis of SCLC, during the last two treatment cycles of carboplatin plus etoposide, NSE levels showed an initial decrease and then a steep increase, while CEA remained stable, indicating eventual chemoresistance and progression of the SCLC subpopulation, confirmed by pathology analysis of a new, recurrent metastatic lymph node biopsy (collected January 2020; Figures S6F and S6G). This compassionate case therefore demonstrates that therapeutic screening of FUTCs can be used to identify effective treatments, many of which cannot otherwise be predicted based on molecular diagnostics, in an individualized manner.

DISCUSSION

Major advances have been made in the past decade in the area of precision cancer medicine and the development of diagnostic innovations, which includes solutions for the *ex vivo* propagation of carcinoma cells. However, unlike murine tumor cells, which generally adapt well to primary cultures, the majority of the patient-derived cultures we established represented non-malignant cells, corroborating conclusions from other recent studies.[17,19,20] While the success rates of establishing cultures from pleural effusion are reportedly higher,[4,13] their use is limited, as only ~10% of all NSCLC patients present with malignant pleural effusions.[36] Other preclinical models such as tumor organoids or xenografts also have suboptimal success rates of 20%–70% or 30%–40%, respectively,[11,15,16,40,41] but these have an additional issue of long establishment times of 1–3 months for organoids or 2–10 months for xenografts.[4,11,15,16,40] Prolonged *ex vivo* propagation in artificial conditions may cause a functional drift of cancer cells from their original identity, and also the patient's tumor may evolve during this time, further compromising the compatibility of preclinical cultures with the diagnostic clinical decision-making process.

To overcome such limitations, and inspired by precision medicine approaches using liquid biopsy-sampled leukemic cells, we set out to assess whether uncultured tumor cell populations could be used for pharmacological profiling immediately following isolation, before their attachment to cell culture plates—the FUTC approach. We asked whether the study of epithelial cells in solution may be compromised (e.g., due to apoptotic priming related to anoikis). Encouragingly, both murine and human FUTCs demonstrated sustained or increased cell viability during the first 3 days of *ex vivo* culture. In addition, murine *Kras* mutant FUTCs were shown to mimic the MEKi-associated resistance bypass mechanisms and related drug sensitivities previously identified in primary cultures derived from these models. These validating findings supported further translational implementation of the approach, and target-matched drug responses were confirmed in FUTCs derived from surgical tissue samples carrying mutant *EGFR*, *MET*, or *RAS*, or rearrangement in *ALK*, with a positive correlation between cancer cell percentage and drug screen data quality. In KRAS-driven tumors, heterogeneity was observed at both inter- and intratumoral levels, which could be explained by underlying differences in biologies such as co-occurring mutations,[26] metabolic dependencies explained (for example) by *KRAS* allelic copy gains,[42] or

(H) Dose-response curves and DSS bar graph of TR, navitoclax (NA), and combination treatment. For the combination screen, 5 nM of TR was used together with the dose series of NA.

(I) Immunoblots of PLT87-derived *KRAS* mutant FUTCs treated with vehicle (C; DMSO) and or treated with 50 nM TR for various time points (4, 24, 48, and 72 h), and probed with indicated antibodies.

Error bars represent ±SEM. Two-tailed unpaired Student's t test: *p < 0.05, **p < 0.01, ***p < 0.001.

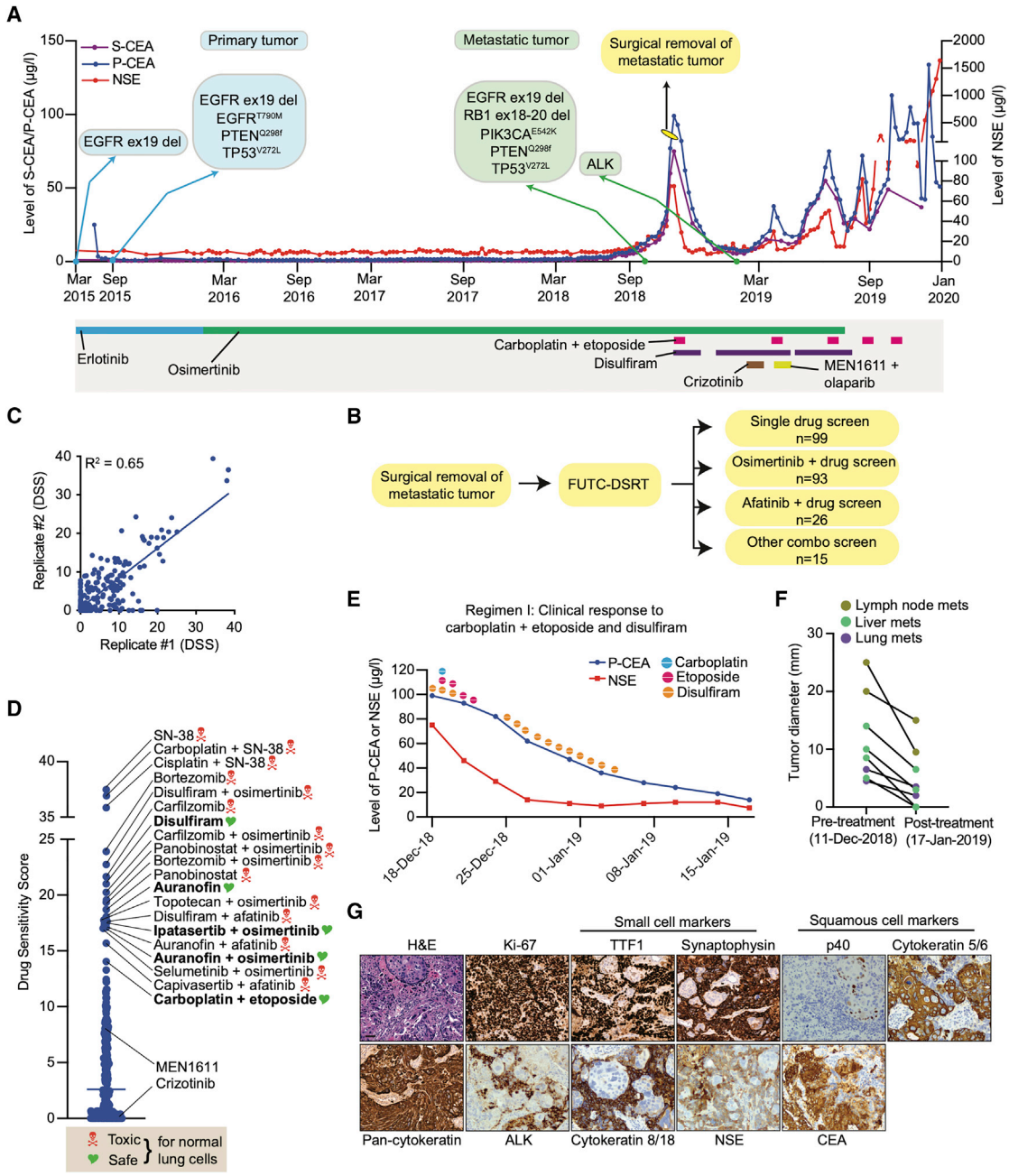

Figure 6. FUTC-based functional testing guided treatment of a patient with refractory lung adenocarcinoma

(A) Treatment outline and measured CSE and NSA levels of a patient with *EGFR* mutant lung adenocarcinoma.

(B) A surgically removed tissue specimen was used for FUTC-based drug testing of 233 single drugs or drug combinations in duplicate.

(C) Correlation plot comparing the DSS from the 2 replicate tests.

(D) The drug sensitivity scores of the top 20 hits, with general toxicity based on activity on normal cells noted.

(E and F) Changes in the level of CEA and NSE (E) and (F) tumor size after carboplatin plus etoposide treatment.

(G) Representative images of hematoxylin and eosin (H&E) and IHC staining performed on surgically resected tumor tissue.

phenotypes influenced by the tumor progenitor cells, such as tumor histopathology or oncogenic signaling activities.[10,21] These data overall indicate that the FUTC assay holds promise for further diagnostic development, particularly for samples with high cancer cellularity. Nevertheless, for samples exhibiting lower cancer cellularity, a number of options can be explored to enhance the data reliability, for example, increasing the number of cells/well, increasing the number of concentration points per drug or technical replicates/compound, or testing multiple drugs for a particular target.

In previous studies, *ex vivo* drug-response testing on heterogeneous primary cancer and stromal cell mixtures failed to culminate in clinical benefits, possibly because these earlier assays did not involve the enrichment of tumor cells.[43,44] In the FUTC assay, cancer cell-selective drug profiling is rather done on EpCAM$^+$ epithelial cells isolated from tumor tissue, with parallel analysis of epithelial cells from adjacent normal tissue serving as a toxicity indicator. A recent study relatedly demonstrated that dynamic BH3 protein profiling reliably reveals drug-elicited apoptotic pathway signaling in freshly isolated breast and colorectal cancer tumor cells, further underscoring our conclusions.[45] A caveat of the FUTC approach is that not all tumor epithelia express EpCAM, with 40%–85% of ACs and 85%–98% of SCCs reported to be EpCAM$^+$.[46–49] To circumvent this, we believe that EpCAM$^-$ cancer cells can be enriched by the use of magnetic microbeads labeled with a cocktail of antibodies that will identify cells of epithelial origin (e.g., cytokeratin 8, cytokeratin 18).[13] Nevertheless, in our dataset, 13 of 19 tumor tissue samples (68%) showed high EpCAM expression levels. Interestingly, genotype-matched drug sensitivities were observed in samples exhibiting moderate to low EpCAM expression levels. In addition, tested samples (8 of 8) showed enrichment of cancer cells following EpCAM selection, and while alternative purification methods are being investigated, EpCAM remains the gold standard for the capture of blood-circulating tumor cells.[50–52] Implementing the EpCAM approach, reliable drug-response data, often matched to the targeted drivers, was obtained from 19 of 20 cases, highlighting the robustness of the assay. Even for drug screens exhibiting Z′ factor values <0.5, we observed reliable dose-response data and genotype-selective drug sensitivities in respective samples. While our preliminary results suggest that the FUTC approach can be adapted to smaller biopsy samples, rigorous investigation is necessary to further optimize its diagnostic utility.

The FUTC assay was implemented to guide the compassionate treatment of a stage IV *EGFR* mutant lung AC patient, with cells derived from an operable metastatic tumor in the neck area. While on EGFR inhibitor treatment, the patient had developed an aggressive disease with multiple metastatic lesions and genomic alterations in, among others, *TP53*, *RB1*, *PIK3CA*, and *PTEN*, commonly associated with EGFR inhibitor resistance. Even though the combined *TP53* and *RB1* mutations may have suggested a risk for histological transformation to SCLC,[36,52] the official diagnosis was AC at the time of FUTC profiling. Nevertheless, in light of FUTC-based drug sensitivity data and the identified mutations, the patient received carboplatin plus etoposide treatment, generally recommended for the treatment of SCLC patients,[19] leading to a substantial reduction in tumor burden and level of tumor markers. As far as we know, this represented a rare clinical case, with only one other report describing dual transformation of *EGFR* mutant lung ACs to NSE-marked SCLC and CEA-marked SCC.[53] These cell populations were found intermixed in the biopsy sample, as if coexisting in symbiosis, perhaps implying that these were derived from a common progenitor cell. In addition to chemotherapy, the patient received another FUTC-guided treatment, the acetaldehyde dehydrogenase (ALDH2) inhibitor disulfiram, but its dosing was reduced as it is associated with delirium, possibly because the patient carried a variant ALDH2*2 allele.[54] The *ex vivo* approach also affirmed the previously known resistance to EGFR inhibitors and it prospectively predicted the non-responses to PI3K and ALK inhibitors, for which the patient was later treated based on molecular features. FUTC-based drug testing therefore both predicted the intrinsic resistance and sensitivity to clinically actionable regimens of the cancer.

This work demonstrates that tumor-derived FUTCs have promise for clinical application. The fast throughput nature of the assay, bypass of *ex vivo* culture, and ability to guide personalized treatment choices render the assay attractive for wider diagnostic use. However, to more broadly assess the clinical feasibility, more clinical profiling cases would need to be actioned, particularly for tumors that lack targetable drivers or metastatic-stage tumors that lack treatment options. It is important to note that since FUTCs allow for the identification of effective combinatorial treatments, the assay can be used to assess polytherapy options to circumvent the emergence of resistance to single treatments. Aligning with our findings, a Phase I clinical trial to test the safety of a triple combination of osimertinib, platinum, and etoposide to circumvent small cell conversion is under way for *EGFR* mutant patients (NCT03567642). In conclusion, FUTC-based functional profiling enables rapid assessment of tumor-selective drug responses and shows promise for further development as a personalized diagnostic assay to complement genomic and histopathological profiling.

Limitations of the study

While our study shows promising results for the FUTC drug screening approach, there are aspects that require further studies for broader application. First, the cancer cellularity of the profiled solid tumor tissue samples affect the drug screen data quality, and this can limit profiling success in some cases. Second, although our preliminary data using a smaller biopsy sample showed promise, this study aspect demands more extensive exploration to transform the FUTC approach into a routine diagnostic test. Finally, the translational functional diagnostic potential of the FUTC assay requires systematic validation in a clinical study.

STAR★METHODS

Detailed methods are provided in the online version of this paper and include the following:

- KEY RESOURCES TABLE
- RESOURCE AVAILABILITY
  - Lead contact
  - Materials availability
  - Data and code availability
- EXPERIMENTAL MODEL AND SUBJECT DETAILS
  - Cell lines
  - Animals
  - Preparation of murine lung-tumor derived FUTCs
  - Patient sample processing
  - CR cultures
- METHOD DETAILS
  - DSRT assay for murine NSCLC models

- DSRT of patient-derived cells
- Western blotting
- Immunohistochemistry (IHC) analyses

- QUANTIFICATION AND STATISTICAL ANALYSIS
  - DSRT data analysis
  - Genomic sequencing and data analysis
  - NGS analysis of lung cancer biopsies
  - KRAS mutation analysis
  - Statistical analyses

SUPPLEMENTAL INFORMATION

Supplemental information can be found online at https://doi.org/10.1016/j.xcrm.2021.100373.

ACKNOWLEDGMENTS

We dedicate this work to the memory of Dyanne Søraas, whose courage and willpower continues to inspire us to advance lung cancer diagnostics and treatment. We acknowledge all of the patients who supported our research by consenting access to clinical specimens. We are thankful to Matti Kankainen and Soili Kytölä for advice on the analysis of next-generation sequencing (NGS) and droplet digital PCR (ddPCR) data, Merja Räsänen for processing patient consents, Ashwini Yadav for assistance on *KRAS* mutation-drug-response association analysis, Astrid Murumägi for reagents and guidance on the establishment of the CR culture protocol, and Vishal Sinha for assistance in drug-response correlation analysis. We thank the Sequencing Core Facility at FIMM, HiLIFE, at the University of Helsinki for NGS analysis, and the Laboratory of Genetics, HUS Diagnostic Center, HUSLAB, at the Helsinki University Hospital for NGS and ddPCR analysis. We thank the HiLIFE Laboratory Animal Centre Core Facility at the University of Helsinki for animal husbandry care and guidance. We thank the thoracic pathologists who helped with the clinical specimen selection, the Laboratory Animal Centre for husbandry support, the FIMM WebMicroscope facility for scanning histological slides, and the FIMM High-Throughput Biomedicine facility for drug screening resources. We thank members of the Verschuren and Wennerberg labs for support and guidance. The study received financial support from the University of Helsinki Integrative Life Science doctoral program (S.S.T.); the Ida Montinin Foundation (S.S.T.); the Väinö and Laina Kivi Foundation (S.S.T.); HUSLAB and the Finnish Medical Foundation (M.I.M.); the Academy of Finland (E.W.V.; grants 307111 and 328473); the Novo Nordisk Foundation (K.W.; the Novo Nordisk Foundation Center for Stem Cell Biology, DanStem; grant no. NNF17CC0027852); and a HiPOC 2020 grant from the University of Helsinki (E.W.V.). The Verschuren lab receives funding from the European Union's Horizon 2020 research and innovation programme under the Marie Skłodowska-Curie grant agreement no. 859860 and the iCAN Digital Precision Cancer Medicine Flagship, Helsinki, Finland.

AUTHOR CONTRIBUTIONS

S.S.T., K.W., and E.W.V. conceived and designed the study; S.S.T. performed experiments for the development of the FUTC-based drug screening assay; J.B., A.H., and N.L. performed the experiments related to the IHC analysis; S.S.T., S.P., and J.B. performed the data analyses; L.S. advised on the compassionate case study design; S.S.T., E.W.V., and K.W. conducted the data interpretation; J.R., A.K., and M.I.M. assisted in collecting the clinical data and the primary tissue workflow, and received patients' consents; M.I.M. and J.L. performed the clinical pathology analyses; and S.S.T., K.W., and E.W.V. wrote the manuscript.

DECLARATION OF INTERESTS

The authors declare no competing interests.

Received: July 8, 2020
Revised: April 20, 2021
Accepted: July 20, 2021
Published: August 17, 2021

REFERENCES

1. Francies, H.E., McDermott, U., and Garnett, M.J. (2020). Genomics-guided pre-clinical development of cancer therapies. Nat. Cancer *1*, 482–492.
2. Tannock, I.F., and Hickman, J.A. (2019). Molecular screening to select therapy for advanced cancer? Ann. Oncol. *30*, 661–663.
3. van der Velden, D.L., Hoes, L.R., van der Wijngaart, H., van Berge Henegouwen, J.M., van Werkhoven, E., Roepman, P., Schilsky, R.L., de Leng, W.W.J., Huitema, A.D.R., Nuijen, B., et al. (2019). The Drug Rediscovery protocol facilitates the expanded use of existing anticancer drugs. Nature *574*, 127–131.
4. Crystal, A.S., Shaw, A.T., Sequist, L.V., Friboulet, L., Niederst, M.J., Lockerman, E.L., Frias, R.L., Gainor, J.F., Amzallag, A., Greninger, P., et al. (2014). Patient-derived models of acquired resistance can identify effective drug combinations for cancer. Science *346*, 1480–1486.
5. Lee, J.K., Liu, Z., Sa, J.K., Shin, S., Wang, J., Bordyuh, M., Cho, H.J., Elliott, O., Chu, T., Choi, S.W., et al. (2018). Pharmacogenomic landscape of patient-derived tumor cells informs precision oncology therapy. Nat. Genet. *50*, 1399–1411.
6. Snijder, B., Vladimer, G.I., Krall, N., Miura, K., Schmolke, A.S., Kornauth, C., Lopez de la Fuente, O., Choi, H.S., van der Kouwe, E., Gültekin, S., et al. (2017). Image-based ex-vivo drug screening for patients with aggressive haematological malignancies: interim results from a single-arm, open-label, pilot study. Lancet Haematol. *4*, e595–e606.
7. Pemovska, T., Kontro, M., Yadav, B., Edgren, H., Eldfors, S., Szwajda, A., Almusa, H., Bespalov, M.M., Ellonen, P., Elonen, E., et al. (2013). Individualized systems medicine strategy to tailor treatments for patients with chemorefractory acute myeloid leukemia. Cancer Discov. *3*, 1416–1429.
8. Tyner, J.W., Yang, W.F., Bankhead, A., 3rd, Fan, G., Fletcher, L.B., Bryant, J., Glover, J.M., Chang, B.H., Spurgeon, S.E., Fleming, W.H., et al. (2013). Kinase pathway dependence in primary human leukemias determined by rapid inhibitor screening. Cancer Res. *73*, 285–296.
9. Davies, E.J., Dong, M., Gutekunst, M., Närhi, K., van Zoggel, H.J., Blom, S., Nagaraj, A., Metsalu, T., Oswald, E., Erkens-Schulze, S., et al. (2015). Capturing complex tumour biology in vitro: histological and molecular characterisation of precision cut slices. Sci. Rep. *5*, 17187.
10. Närhi, K., Nagaraj, A.S., Parri, E., Turkki, R., van Duijn, P.W., Hemmes, A., Lahtela, J., Uotinen, V., Mäyränpää, M.I., Salmenkivi, K., et al. (2018). Spatial aspects of oncogenic signalling determine the response to combination therapy in slice explants from Kras-driven lung tumours. J. Pathol. *245*, 101–113.
11. Pauli, C., Hopkins, B.D., Prandi, D., Shaw, R., Fedrizzi, T., Sboner, A., Sailer, V., Augello, M., Puca, L., Rosati, R., et al. (2017). Personalized *In Vitro* and *In Vivo* Cancer Models to Guide Precision Medicine. Cancer Discov. *7*, 462–477.
12. Friedman, A.A., Letai, A., Fisher, D.E., and Flaherty, K.T. (2015). Precision medicine for cancer with next-generation functional diagnostics. Nat. Rev. Cancer *15*, 747–756.
13. Kodack, D.P., Farago, A.F., Dastur, A., Held, M.A., Dardaei, L., Friboulet, L., von Flotow, F., Damon, L.J., Lee, D., Parks, M., et al. (2017). Primary patient-derived cancer cells and their potential for personalized cancer patient care. Cell Rep. *21*, 3298–3309.
14. Yuan, H., Myers, S., Wang, J., Zhou, D., Woo, J.A., Kallakury, B., Ju, A., Bazylewicz, M., Carter, Y.M., Albanese, C., et al. (2012). Use of reprogrammed cells to identify therapy for respiratory papillomatosis. N. Engl. J. Med. *367*, 1220–1227.
15. Kim, M., Mun, H., Sung, C.O., Cho, E.J., Jeon, H.J., Chun, S.M., Jung, D.J., Shin, T.H., Jeong, G.S., Kim, D.K., et al. (2019). Patient-derived

lung cancer organoids as in vitro cancer models for therapeutic screening. Nat. Commun. *10*, 3991.

16. Shi, R., Radulovich, N., Ng, C., Liu, N., Notsuda, H., Cabanero, M., Martins-Filho, S.N., Raghavan, V., Li, Q., Mer, A.S., et al. (2020). Organoid cultures as preclinical models of non-small cell lung cancer. Clin. Cancer Res. *26*, 1162–1174.
17. Gao, B., Huang, C., Kernstine, K., Pelekanou, V., Kluger, Y., Jiang, T., Peters-Hall, J.R., Coquelin, M., Girard, L., Zhang, W., et al. (2017). Non-malignant respiratory epithelial cells preferentially proliferate from resected non-small cell lung cancer specimens cultured under conditionally reprogrammed conditions. Oncotarget *8*, 11114–11126.
18. Liu, X., Ory, V., Chapman, S., Yuan, H., Albanese, C., Kallakury, B., Timofeeva, O.A., Nealon, C., Dakic, A., Simic, V., et al. (2012). ROCK inhibitor and feeder cells induce the conditional reprogramming of epithelial cells. Am. J. Pathol. *180*, 599–607.
19. Yu, F., Lu, Y., Tao, L., Jiang, Y.Y., Lin, D.C., Wang, L., Petersson, F., Yoshiyama, H., Koeffler, P.H., Goh, B.C., and Loh, K.S. (2017). Non-malignant epithelial cells preferentially proliferate from nasopharyngeal carcinoma biopsy cultured under conditionally reprogrammed conditions. Sci. Rep. *7*, 17359.
20. Sette, G., Salvati, V., Giordani, I., Pilozzi, E., Quacquarini, D., Duranti, E., De Nicola, F., Pallocca, M., Fanciulli, M., Falchi, M., et al. (2018). Conditionally reprogrammed cells (CRC) methodology does not allow the in vitro expansion of patient-derived primary and metastatic lung cancer cells. Int. J. Cancer *143*, 88–99.
21. Nagaraj, A.S., Lahtela, J., Hemmes, A., Pellinen, T., Blom, S., Devlin, J.R., Salmenkivi, K., Kallioniemi, O., Mäyränpää, M.I., Närhi, K., and Verschuren, E.W. (2017). Cell of origin links histotype spectrum to immune microenvironment diversity in non-small-cell lung cancer driven by mutant KRAS and loss of Lkb1. Cell Rep. *18*, 673–684.
22. Talwelkar, S.S., Nagaraj, A.S., Devlin, J.R., Hemmes, A., Potdar, S., Kiss, E.A., Saharinen, P., Salmenkivi, K., Mäyränpää, M.I., Wennerberg, K., and Verschuren, E.W. (2019). Receptor tyrosine kinase signaling networks define sensitivity to erbb inhibition and stratify *Kras*-mutant lung cancers. Mol. Cancer Ther. *18*, 1863–1874.
23. Liu, K., Guo, J., Liu, K., Fan, P., Zeng, Y., Xu, C., Zhong, J., Li, Q., and Zhou, Y. (2018). Integrative analysis reveals distinct subtypes with therapeutic implications in KRAS-mutant lung adenocarcinoma. EBioMedicine *36*, 196–208.
24. Skoulidis, F., Byers, L.A., Diao, L., Papadimitrakopoulou, V.A., Tong, P., Izzo, J., Behrens, C., Kadara, H., Parra, E.R., Canales, J.R., et al. (2015). Co-occurring genomic alterations define major subsets of KRAS-mutant lung adenocarcinoma with distinct biology, immune profiles, and therapeutic vulnerabilities. Cancer Discov. *5*, 860–877.
25. Kitai, H., Ebi, H., Tomida, S., Floros, K.V., Kotani, H., Adachi, Y., Oizumi, S., Nishimura, M., Faber, A.C., and Yano, S. (2016). Epithelial-to-mesenchymal transition defines feedback activation of receptor tyrosine kinase signaling induced by MEK inhibition in KRAS-mutant lung cancer. Cancer Discov. *6*, 754–769.
26. Kruspig, B., Monteverde, T., Neidler, S., Hock, A., Kerr, E., Nixon, C., Clark, W., Hedley, A., Laing, S., Coffelt, S.B., et al. (2018). The ERBB network facilitates KRAS-driven lung tumorigenesis. Sci. Transl. Med. *10*, eaao2565.
27. Masuzawa, K., Yasuda, H., Hamamoto, J., Nukaga, S., Hirano, T., Kawada, I., Naoki, K., Soejima, K., and Betsuyaku, T. (2017). Characterization of the efficacies of osimertinib and nazartinib against cells expressing clinically relevant epidermal growth factor receptor mutations. Oncotarget *8*, 105479–105491.
28. Soria, J.C., Ohe, Y., Vansteenkiste, J., Reungwetwattana, T., Chewaskulyong, B., Lee, K.H., Dechaphunkul, A., Imamura, F., Nogami, N., Kurata, T., et al.; FLAURA Investigators (2018). Osimertinib in untreated EGFR-mutated advanced non-small-cell lung cancer. N. Engl. J. Med. *378*, 113–125.
29. Hirano, T., Yasuda, H., Tani, T., Hamamoto, J., Oashi, A., Ishioka, K., Arai, D., Nukaga, S., Miyawaki, M., Kawada, I., et al. (2015). In vitro modeling to determine mutation specificity of EGFR tyrosine kinase inhibitors against clinically relevant EGFR mutants in non-small-cell lung cancer. Oncotarget *6*, 38789–38803.
30. Lee, Y., Kim, T.M., Kim, D.W., Kim, S., Kim, M., Keam, B., Ku, J.L., and Heo, D.S. (2019). Preclinical Modeling of Osimertinib for NSCLC With EGFR Exon 20 Insertion Mutations. J. Thorac. Oncol. *14*, 1556–1566.
31. Fukuda, K., Takeuchi, S., Arai, S., Katayama, R., Nanjo, S., Tanimoto, A., Nishiyama, A., Nakagawa, T., Taniguchi, H., Suzuki, T., et al. (2019). Epithelial-to-mesenchymal transition is a mechanism of ALK inhibitor resistance in lung cancer independent of *ALK* mutation status. Cancer Res. *79*, 1658–1670.
32. Kim, H.R., Kim, W.S., Choi, Y.J., Choi, C.M., Rho, J.K., and Lee, J.C. (2013). Epithelial-mesenchymal transition leads to crizotinib resistance in H2228 lung cancer cells with EML4-ALK translocation. Mol. Oncol. *7*, 1093–1102.
33. Yang, W., Soares, J., Greninger, P., Edelman, E.J., Lightfoot, H., Forbes, S., Bindal, N., Beare, D., Smith, J.A., Thompson, I.R., et al. (2013). Genomics of Drug Sensitivity in Cancer (GDSC): a resource for therapeutic biomarker discovery in cancer cells. Nucleic Acids Res. *41*, D955–D961.
34. Krall, E.B., Wang, B., Munoz, D.M., Ilic, N., Raghavan, S., Niederst, M.J., et al. (2017). KEAP1 loss modulates sensitivity to kinase targeted therapy in lung cancer. eLife *6*, e18970.
35. Corcoran, R.B., Cheng, K.A., Hata, A.N., Faber, A.C., Ebi, H., Coffee, E.M., Greninger, P., Brown, R.D., Godfrey, J.T., Cohoon, T.J., et al. (2013). Synthetic lethal interaction of combined BCL-XL and MEK inhibition promotes tumor regressions in KRAS mutant cancer models. Cancer Cell *23*, 121–128.
36. Niederst, M.J., Sequist, L.V., Poirier, J.T., Mermel, C.H., Lockerman, E.L., Garcia, A.R., Katayama, R., Costa, C., Ross, K.N., Moran, T., et al. (2015). RB loss in resistant EGFR mutant lung adenocarcinomas that transform to small-cell lung cancer. Nat. Commun. *6*, 6377.
37. Chen, Y., Tang, W.Y., Tong, X., and Ji, H. (2019). Pathological transition as the arising mechanism for drug resistance in lung cancer. Cancer Commun. (Lond.) *39*, 53.
38. Chan, B.A., and Coward, J.I. (2013). Chemotherapy advances in small-cell lung cancer. J. Thorac. Dis. *5* (*Suppl 5*), S565–S578.
39. Marcoux, N., Gettinger, S.N., O'Kane, G., Arbour, K.C., Neal, J.W., Husain, H., Evans, T.L., Brahmer, J.R., Muzikansky, A., Bonomi, P.D., et al. (2019). EGFR-Mutant Adenocarcinomas That Transform to Small-Cell Lung Cancer and Other Neuroendocrine Carcinomas: Clinical Outcomes. J. Clin. Oncol. *37*, 278–285.
40. Tentler, J.J., Tan, A.C., Weekes, C.D., Jimeno, A., Leong, S., Pitts, T.M., Arcaroli, J.J., Messersmith, W.A., and Eckhardt, S.G. (2012). Patient-derived tumour xenografts as models for oncology drug development. Nat. Rev. Clin. Oncol. *9*, 338–350.
41. Dijkstra, K.K., Monkhorst, K., Schipper, L.J., Hartemink, K.J., Smit, E.F., Kaing, S., de Groot, R., Wolkers, M.C., Clevers, H., Cuppen, E., and Voest, E.E. (2020). Challenges in Establishing Pure Lung Cancer Organoids Limit Their Utility for Personalized Medicine. Cell Rep. *31*, 107588.
42. Kerr, E.M., Gaude, E., Turrell, F.K., Frezza, C., and Martins, C.P. (2016). Mutant Kras copy number defines metabolic reprogramming and therapeutic susceptibilities. Nature *531*, 110–113.
43. Burstein, H.J., Mangu, P.B., Somerfield, M.R., Schrag, D., Samson, D., Holt, L., Zelman, D., and Ajani, J.A.; American Society of Clinical Oncology (2011). American Society of Clinical Oncology clinical practice guideline update on the use of chemotherapy sensitivity and resistance assays. J. Clin. Oncol. *29*, 3328–3330.
44. Schrag, D., Garewal, H.S., Burstein, H.J., Samson, D.J., Von Hoff, D.D., and Somerfield, M.R.; ASCO Working Group on Chemotherapy Sensitivity and Resistance Assays (2004). American Society of Clinical Oncology

Technology Assessment: chemotherapy sensitivity and resistance assays. J. Clin. Oncol. *22*, 3631–3638.

45. Bhola, P.D., Ahmed, E., Guerriero, J.L., Sicinska, E., Su, E., Lavrova, E., Ni, J., Chipashvili, O., Hagan, T., Pioso, M.S., et al. (2020). High-throughput dynamic BH3 profiling may quickly and accurately predict effective therapies in solid tumors. Sci. Signal. *13*, eaay1451.
46. Piyathilake, C.J., Frost, A.R., Weiss, H., Manne, U., Heimburger, D.C., and Grizzle, W.E. (2000). The expression of Ep-CAM (17-1A) in squamous cell cancers of the lung. Hum. Pathol. *31*, 482–487.
47. Went, P.T., Lugli, A., Meier, S., Bundi, M., Mirlacher, M., Sauter, G., and Dirnhofer, S. (2004). Frequent EpCam protein expression in human carcinomas. Hum. Pathol. *35*, 122–128.
48. Kim, Y., Kim, H.S., Cui, Z.Y., Lee, H.S., Ahn, J.S., Park, C.K., Park, K., and Ahn, M.J. (2009). Clinicopathological implications of EpCAM expression in adenocarcinoma of the lung. Anticancer Res. *29*, 1817–1822.
49. Pak, M.G., Shin, D.H., Lee, C.H., and Lee, M.K. (2012). Significance of EpCAM and TROP2 expression in non-small cell lung cancer. World J. Surg. Oncol. *10*, 53.
50. Krebs, M.G., Hou, J.M., Sloane, R., Lancashire, L., Priest, L., Nonaka, D., Ward, T.H., Backen, A., Clack, G., Hughes, A., et al. (2012). Analysis of circulating tumor cells in patients with non-small cell lung cancer using epithelial marker-dependent and -independent approaches. J. Thorac. Oncol. *7*, 306–315.
51. Bidard, F.C., Peeters, D.J., Fehm, T., Nolé, F., Gisbert-Criado, R., Mavroudis, D., Grisanti, S., Generali, D., Garcia-Saenz, J.A., Stebbing, J., et al. (2014). Clinical validity of circulating tumour cells in patients with metastatic breast cancer: a pooled analysis of individual patient data. Lancet Oncol. *15*, 406–414.
52. Offin, M., Chan, J.M., Tenet, M., Rizvi, H.A., Shen, R., Riely, G.J., Rekhtman, N., Daneshbod, Y., Quintanal-Villalonga, A., Penson, A., et al. (2019). Concurrent RB1 and TP53 Alterations Define a Subset of EGFR-Mutant Lung Cancers at risk for Histologic Transformation and Inferior Clinical Outcomes. J. Thorac. Oncol. *14*, 1784–1793.
53. Yao, Y., Zhu, Z., Wu, Y., and Chai, Y. (2018). Histologic transformation from adenocarcinoma to both small cell lung cancer and squamous cell carcinoma after treatment with gefitinib: a case report. Medicine (Baltimore) *97*, e0650.
54. Jin, S., Chen, J., Chen, L., Histen, G., Lin, Z., Gross, S., Hixon, J., Chen, Y., Kung, C., Chen, Y., et al. (2015). ALDH2(E487K) mutation increases protein turnover and promotes murine hepatocarcinogenesis. Proc. Natl. Acad. Sci. USA *112*, 9088–9093.
55. Bao, J., Walliander, M., Kovács, F., Nagaraj, A.S., Hemmes, A., Sarhadi, V.K., Knuutila, S., Lundin, J., Horvath, P., and Verschuren, E.W. (2019). Spa-RQ: An Image Analysis Tool to Visualise and Quantify Spatial Phenotypes Applied to Non-Small Cell Lung Cancer. Sci. Rep. *9*, 17613.
56. Dufva, O., Kankainen, M., Kelkka, T., Sekiguchi, N., Awad, S.A., Eldfors, S., Yadav, B., Kuusanmäki, H., Malani, D., Andersson, E.I., et al. (2018). Aggressive natural killer-cell leukemia mutational landscape and drug profiling highlight JAK-STAT signaling as therapeutic target. Nat. Commun. *9*, 1567.
57. Potdar, S., Ianevski, A., Mpindi, J.P., Bychkov, D., Fiere, C., Ianevski, P., Yadav, B., Wennerberg, K., Aittokallio, T., Kallioniemi, O., et al. (2020). Breeze: an integrated quality control and data analysis application for high-throughput drug screening. Bioinformatics *36*, 3602–3604.
58. Yadav, B., Pemovska, T., Szwajda, A., Kulesskiy, E., Kontro, M., Karjalainen, R., Majumder, M.M., Malani, D., Murumägi, A., Knowles, J., et al. (2014). Quantitative scoring of differential drug sensitivity for individually optimized anticancer therapies. Sci. Rep. *4*, 5193.

STAR★METHODS

KEY RESOURCES TABLE

REAGENT or RESOURCE	SOURCE	IDENTIFIER
Antibodies		
p63	Abcam	Cat#ab124762; RRID: AB_10971840
NKX2-1	Abcam	Cat#ab133638; RRID: AB_2734144
LKB1	Cell Signaling Technology	Cat#13031; RRID: AB_2716796
Ki-67	Thermo Fisher Scientific	RM-9106-S0; RRID: AB_2341197
pERK (Thr202/Tyr204)	Cell Signaling Technology	Cat#4370; RRID: AB_2315112
pAKT (Ser473)	Cell Signaling Technology	Cat#4060; RRID: AB_2315049
p4EBP1 (Thr37/46)	Cell Signaling Technology	Cat#2855; RRID :AB_560835
E-cadherin	Cell Signaling Technology	Cat#3195; RRID: AB_2291471
Vimentin	Abcam	Cat#ab92547; RRID: AB_10562134
pEGFR (Tyr 1068)	Cell Signaling Technology	Cat#2234; RRID: AB_331701
pERBB2 (Tyr1211/1222)	Cell Signaling Technology	Cat#2243; RRID: AB_490899
pERBB3 (Tyr1289)	Cell Signaling Technology	Cat#4791; RRID: AB_2099709
α-Tubulin	Cell Signaling Technology	Cat#2125; RRID: AB_2619646
AKT	Cell Signaling Technology	Cat#2920; RRID: AB_1147620
ERK	Cell Signaling Technology	Cat#9107; RRID: AB_10695739
ALK	Cell Signaling Technology	Cat#3633; RRID: AB_11127207
EpCAM	Abcam	Cat#71916; RRID: AB_1603782
Biological samples		
CR cultures derived from murine NSCLC tumors obtained from $Kras^{G12D}$;$Lkb1^{fl/fl}$ (KL) mouse model	This Paper	N/A
FUTCs derived from murine NSCLC tumors obtained from $Kras^{G12D}$;$p53^{fl/fl}$ (KP) mouse model	This Paper	N/A
CR cultures derived from murine NSCLC tumors obtained from $Kras^{G12D}$;$p53^{fl/fl}$ (KP) mouse model	This Paper	N/A
Human normal lung CR cultures derived from tumor-adjacent normal lung tissue lung	This Paper	N/A
Human lung tumor-derived fresh uncultured tumor cells	This Paper	N/A
Chemicals, peptides, and recombinant proteins		
Collagenase	Sigma	Cat#C2674-1G
Dispase	Invitrogen	Cat#17105041
BSA	Sigma	Cat#A2153
EpCAM (CD326) MicroBeads, mouse	Miltenyi Biotec	Cat#130-105-958
DMEM	GIBCO	Cat#42430-025
F12	GIBCO	Cat#21765-029
Y-27632, ROCK inhibitor	ENZO life sciences	Cat#ALX-270-333-M005
Adenine	Sigma	Cat#A2786
hrEGF	BD Bioscience	Cat#354052
Insulin	Sigma	Cat#I2643
Hydrocortisone	Sigma	Cat#H4001
Cholera toxin	List Biological laboratory	Cat#100B
CellTiter-Glo	Promega	Cat#G9243
EpCAM (CD326) MicroBeads, human	Miltenyi Biotec	Cat#130-061-101
Polyacrylamide gels, 4–20%	Bio-Rad	Cat#4561096

(*Continued on next page*)

Continued

REAGENT or RESOURCE	SOURCE	IDENTIFIER
HBSS	Sigma	Cat#H6648
Critical commercial assays		
Tumor Dissociation Kit, human	Miltenyi Biotec	Cat#130-095-929
BCA Protein Assay	G Biosciences	Cat#786-570
gentleMACS Dissociator	Miltenyi Biotec	Cat#130-093-235
Deposited data		
Next-generation sequencing data for lung cancer patients	Mendeley Data	https://data.mendeley.com/datasets/bb4vfjnfkf/1
Experimental models: Cell lines		
J2 strain of Swiss-3T3 mouse fibroblasts	Kindly provided by Prof. Olli Kallioniemi at Sci Life Lab	N/A
Experimental models: Organisms/strains		
Mouse: KP: *Kras$^{LSL.G12D/+}$;p53$^{fl/fl}$*	Jackson laboratories	N/A
Mouse: KL: *Kras$^{LSL.G12D/+}$;Lkb1$^{fl/fl}$*	Jackson laboratories and Ron DePinho (MD Anderson).	N/A
Software and algorithms		
BREEZE pipeline	Potdar et al. [55]	https://breeze.fimm.fi/28780_mc40mdewodkwmcaxnje4ode3nje0/index.php
Aiforia	N/A	https://www.aiforia.com/
Spa-RQ	Bao et al. [56]	https://bitbucket.org/MagoBitbucket/spa-rq-tools/downloads/
GDSC	Yang et al.[33]	https://www.cancerrxgene.org/
GraphPad Prism 9.1.0	GraphPad	N/A

RESOURCE AVAILABILITY

Lead contact

Further information and requests for resources and reagents should be directed to and will be fulfilled by the lead contact, Emmy Verschuren (emmy.verschuren@helsinki.fi).

Materials availability

This study did not generate new unique reagents.

Data and code availability

The authors declare that the main data supporting the findings of this study are available within the article. The data presented in Figure S3A of this study are available from the GDSC1 database portal (GDSC: https://www.cancerrxgene.org/). Processed NGS data is available online from the Mendeley Data (Mendeley Data: https://doi.org/10.17632/bb4vfjnfkf.1). Raw NGS data and IHC images generated in this study are available from the lead contact with a completed Materials Transfer Agreement.

EXPERIMENTAL MODEL AND SUBJECT DETAILS

Cell lines

The J2 strain of Swiss-3T3 mouse fibroblasts was kindly provided by Prof. Olli Kallioniemi at SciLifeLab. To culture 3T3 cells, we used DMEM supplemented with 10% FBS and cultures were maintained at 37°C and 5% CO2. 3T3 cells were passaged two to three times per week, and irradiated cells were used as a feeder layer for the propagation of CR cultures until the cells reached passage ten. Cultures were routinely checked for mycoplasma infection.

Animals

Mouse models harboring a conditional Kras mutant allele (KrasLSL-G12D/+) or loss-of-function TRp53 allele (p53fl/fl) were procured from the Jackson laboratories. Mouse models harboring loss-of-function Stk11/Lkb1 allele (Lkb1fl/fl) were received from Ron

DePinho (MD Anderson). Around 10 week old KL and KP mice were intranasally administered with progenitor cell-directed Ad5-Cre viruses.[21] Moribund mice were sacrificed by cervical dislocation, and tumor-bearing lungs were processed for FUTC-based pharmacological profiling. All mice used in this study were housed in the Laboratory Animal Center of the University of Helsinki. The facility provided animal care services including feeding, cage cleaning, health assessment, and room sanitation. Animals of both sexes were utilized for this work.

Preparation of murine lung-tumor derived FUTCs

Experiments involving KP and KL genetically engineered mouse models were conducted following the guidelines from the Finnish National Board of Animal Experimentation (permit number ESAVI/9752/04.10.07/2015) and all procedures were performed as described previously.[21] For FUTC isolation, individual lung tumors were manually minced using a sterile scalpel and then enzymatically digested in HBSS containing 2 mg/ml collagenase, 0.3 mg/ml dispase and 10 mg/ml bovine serum albumin (BSA), using a Miltenyi gentleMACS dissociator, as described.[22] Lung 2.01 program on MACS dissociator was used for cell homogenization and subsequently cells were filtered 70 μm cell strainers and centrifuged at 200xg for 10 min at 4°C. To separate EpCAM+ cells from tumor tissue dissociates, EpCAM (CD326) MicroBeads-dependent enrichment was implemented (130-105-958, MACS), as per the manufacturer's instructions. Briefly, single cells obtained from tumor tissue were incubated for 15 minutes with EpCAM (CD326) microbeads in the refrigerator (2-8°C). These EpCAM microbead-labeled cells were subjected to magnetic separation using MACS LS Columns and MACS Magnetic Separator. LS Columns were placed on a Magnetic Separator and EpCAM microbead-labeled cells were applied onto the column. Unlabeled cells were collected in the flow-through while magnetically labeled cells were pushed out of the column using a plunger. These microbead-labeled EpCAM+ FUTCs were then either directly utilized for drug response assessment or for establishment of CR cultures. Detailed CR culture procedures are provided in the CR cultures method section.

Patient sample processing

Clinical samples used in this study were collected with patient's informed consent at the Helsinki University Central Hospital (HUCH) and procedures were conducted in accordance with protocol approved by the Coordinating Ethics Committee of the University of Helsinki (License numbers: 85/13/03/00/2015 and HUS-1204-2019). Clinical features of cases used in this study are shown in Tables 1 and S1. All specimens used in this study were collected from adult patients; gender and age of the patients were not considered as significant factors in this study. To process clinical specimens for FUTC assay, within 30 mins after lobectomy, tumor and tumor-adjacent healthy lung tissue samples were transported from the hospital to the cell culture facility in cold HBSS. The tissue sample was divided into four parts, one each for DNA isolation, lysate preparation for western blot, histological analysis, and FUTC isolation. Subsequently, for single cell suspension, tumor tissue was manually minced using a sterile scalpel, and then enzymatically digested using a Tumor Dissociation Kit (Miltenyi, 130-095-929) and a gentleMACS Dissociator (130-093-235) following the manufacturer's instructions. Single cell suspensions were then subjected to separation of EpCAM+ and EpCAM– cell fractions using Miltenyi's human EpCAM (CD326) MicroBeads (130-061-101). EpCAM+/– cells derived from tumor tissue, and EpCAM+ cells derived from normal tissue were used for performing DSRT.

CR cultures

Both murine and human EpCAM+ cells were propagated using a Conditional Reprogramming (CR) culture protocol. In brief, EpCAM+ cells were plated on irradiated (30 gray) 3T3 cells in F-medium composed of 1:3 v/v DMEM: F-12 nutrient HAM supplemented with 5% FBS, 10 ng/ml EGF (BD Biosciences; 354052), 5 μg/ml insulin (Sigma; I2643), 24 μg/ml adenine (Sigma; A2786), 0.4 μg/ml hydrocortisone (Sigma; H4001), 10 ng/ml cholera toxin (List Biological laboratory; 100B), and 10 μM ROCK inhibitor (Y-27632; ENZO). All CR cultures were maintained at 37°C and 5% CO2. When CR cultures reached 80% confluence, they were differentially trypsinized using a two-step procedure the first to remove loosely attached feeder cells, and the second to trypsinize epithelial cells.

METHOD DETAILS

DSRT assay for murine NSCLC models

Tumor-derived fresh uncultured EpCAM+ cells and CR cultures at passage 4 were used for performing DSRT, as described previously.[22] Briefly, 2500 FUTCs or 1500 CR cells per well were seeded in 384-well plates using a Biotek MultiFlo FX RAD dispenser in 20 μL F-medium. Following 24 h incubation, drugs were manually dispensed in 10 μL F-medium at eight concentrations, covering a 10,000-fold concentration range in triplicates. Additionally, multiple replicates of cells were treated with 0.1% dimethyl sulfoxide (DMSO) or 100 μM benzethonium chloride, serving as negative and positive controls, respectively. Following 72 h incubation at 37°C, 30 μL CellTiter-Glo reagent (Promega) was added in each well, and cell viability was measured using a PheraStar FS plate reader (BMG Labtech).

DSRT of patient-derived cells

To screen 66 lung cancer selective drugs, DSRT plates were prepared in advance by dispensing compounds into 384-well plates (3712, Corning) using an Echo 550 liquid handler (Labcyte), at five concentrations covering a 10,000-fold concentration range. As negative and positive controls, 0.1% DMSO and 100 μM benzethonium chloride were included in wells scattered across the plates. Pressurized Storage Pods (Roylan Developments Ltd.) were used to store pre-drugged DSRT plates and were used within one

month. Tumor- and normal tissue-derived cells (2500 cells per well) were seeded in pre-drugged DSRT plates using a Biotek MultiFlo FX RAD dispenser, in 25 μL F-medium. Following 72 h incubation at 37°C, 25 μL CellTiter-Glo reagent (Promega) was added in each well, and cell viability was measured using a PheraStar FS plate reader (BMG Labtech). When the cell numbers were not sufficient for performing the 66-drug screen, drug screening for molecular target-selective drugs (5 - 10) were performed by seeding 2500 FUTCs/well in 384-well plates, and on the following day cells were exposed to drugs.

For the compassionate care case study, patient-derived tumor cells were directly utilized for DSRT without performing EpCAM-based immunomagnetic separation step as cytological and histological assessment of frozen tumor tissue sections prior to drug testing initiation revealed high (< 90%) cancer cellularity. In brief, tumor tissue within 60 minutes of surgical excision was embedded in Optimal Cutting Temperature (OCT) media and cryosections cut from the OCT block were stained with H&E. Stained sections were analyzed by a clinical pulmonary pathologist.

Western blotting

Reference tumor tissues, FUTC pellets, or CR cell pellets were lysed with RIPA buffer supplemented with fresh protease and phosphatase inhibitors (Roche). For protein quantification, BCA Protein Assay was used (G Biosciences; 786-570). Western blotting was performed using 20 μg of protein samples, using precast 4%–20% polyacrylamide gel (Bio-Rad, 4561096) for electrophoresis and PVDF membrane (Millipore, IPFL00010) for transfer. Western blot membranes were blocked using Odyssey Blocking Buffer (927-40000) at room temperature for 30 min, probed with primary antibodies at room temperature for 2 h or overnight at 4°C, and finally probed with IRDye secondary antibodies (LI-COR) diluted 1:10000 in Odyssey Blocking Buffer and scanned using an Odyssey infrared imager (LI-COR). We used Image Studio Lite software for western blot quantification.

Immunohistochemistry (IHC) analyses

Tissue processing and IHC procedures were performed as described previously[22]; all samples were processed using the equivalent experimental conditions. The Pannoramic 250 digital slide scanner (3DHISTECH, Budapest, Hungary) was used to acquire whole slide scans of stained tumor sections using a 20x objective, and the Pannoramic Viewer (3DHISTECH Ltd) was used at 1:4 magnification to export TIFF images.

To quantify the percentage of malignant epithelial region or cancer cellularity per tumor specimen, H&E stained whole tissue sections were uploaded to the deep learning-based image analysis cloud service, Aiforia (Fimmic Oy, Helsinki, Finland). Regional training sets were manually created by an imaging expert, by selecting regions-of-interest (206 regions) across all H&E-stained samples as two-layer sets, namely a parental layer for whole tumor tissue annotation and a layer for tumor epithelium-only annotation that was further guided by E-Cadherin staining on neighboring sections. The manually annotated tissue regions were used to train the Aiforia algorithm; multiple training-learning cycles were conducted until the predictions on all samples reached a satisfactory outcome. A total of 22 annotations for tissue regions and 184 annotations for tumor epithelial regions were included in the training. The results were validated by a clinical pulmonary pathologist, via the validation functions of Aiforia, and percentages of tumor epithelial regions per specimen were calculated. To quantify the percentage of cancer cells exhibiting EpCAM expression and to classify cancer cells based on the EpCAM intensity, we implemented a two-step process using the Aiforia algorithm. First, based on staining intensity and specificity cells are manually annotated as strongly or weakly positive. The manually annotated tissue regions exhibiting different patterns of EpCAM expression were used to train the Aiforia algorithm; multiple training-learning cycles were conducted until the predictions on all samples reached a satisfactory outcome. In the second step, trained Aiforia algorithm was used to calculate the percentage of cancer cells exhibiting strong or weak EpCAM positivity. To quantify the percentages of proliferating cancer cells, both region- and cell-based annotation tools provided by Aiforia were used. A two-layer training set was created, composed of a parental layer of tumor epithelial regions (based on H&E staining) and a cell-based layer to assign (i) proliferating (Ki-67 positive) and (ii) non-proliferating (Ki-67 negative) tumor cells. Multiple training-learning cycles were performed until the deep-learning prediction reached satisfactory outcome and then percentage of Ki-67 positivity were calculated using total number of proliferating and non-proliferating tumor cells.

To assess MAPK and PI3K-AKT-mTOR signaling pathway activities in tumor regions, images stained with phosphorylated ERK, and 4EBP1 were registered to directly adjacent E-cadherin-stained sections, and the overlap of staining was quantified using a spatial quantification and registration image analysis tool Spa-RQ, as described in Bao et al.[55] To assess the co-activation between MAPK and PI3K-AKT-mTOR signaling pathways, images stained with phosphorylated ERK and 4EBP1 were registered to each other and the region of staining overlap was quantified by Spa-RQ. Spa-RQ employed a simple thresholding segmentation algorithm, a consistent threshold for each staining was applied to all the samples. The staining specificity and accuracy of the Spa-RQ was validated by a clinical pulmonary pathologist. To assess EMT, all tumor tissue sections were visually inspected for co-positivity of E-cadherin and vimentin in tumor epithelium-only regions. Tissue sections stained for phosphorylated EGFR, ERBB2, or ERBB3 proteins were visually inspected for positivity in tumor only regions.

QUANTIFICATION AND STATISTICAL ANALYSIS

DSRT data analysis

To determine screen-to-screen consistency of DSRT profiling, Z-prime factors were calculated by normalizing the raw luminescence values of drug-treated wells with positive and negative controls. Screens showing a Z-prime factor < 0.2 were not considered for

further analysis (one of 20 cases). As we were analyzing dose response series with multiple assay points for each drug, we applied a slightly lower threshold for the Z-prime factor (> 0.2) than the cutoff that is most frequently used in standard high throughput single data point assays (> 0.5). Screens with Z-prime factor values from 0.2 to 0.5 still exhibited sigmoidal dose response curves and data consistency was observed across technical replicates, and with respect to the tumor genotype. Dose-response curves were plotted using a Marquardt-Levenberg algorithm via the in-house bioinformatic 'Breeze' pipeline.[57] Next, dose–response curve parameters were employed to calculate the Drug Sensitivity Score (DSS), as described.[58]

Genomic sequencing and data analysis

A DNeasy Blood & Tissue kit (QIAGEN) was used to extract genomic DNA from healthy lung and tumor tissue samples and from CR cultures (Table 1). Genomic dsDNA (382-500 ng) was fragmented with a Covaris E220 evolution instrument (Covaris) to a mean fragment size of 200 base pairs (bp). For sample library preparation and enrichment, a KAPA Hyper library preparation kit was used, following the SeqCap EZ HyperCap Workflow User's Guide Version 1.0 (Roche Nimblegen). In brief, pre-capture amplification was performed using 9 cycles, and captures were performed in multiplexes of 3 to 4 samples using 0.667-1 μg of each library. To identify somatic mutations, targeted next-generation sequencing was performed using the Illumina HiSeq2500 system in HiSeq high output mode using v4 chemistry or HiSeq Rapid run mode using v2 chemistry (Illumina), with the NimbleGen Cancer Panel to capture the exons of 578 cancer-related genes. NimbleGen probes used were 120522_HG19_Onco_R_EZ. Instead of SeqCap HE-Oligos, we used xGen Universal Blocking oligo TS mix (IDT). For post-capture amplification, ten cycles were used in two replicate reactions. The library was quantified for sequencing using the 2100 Bioanalyzer High sensitivity kit. Read length for the paired-end run was 2x101 bp. Pre-processing of short read data was done using the Trimmomatic software and included correction of the sequence data for adaptor sequences, bases with low quality, and reads less than 36 bp in length. The BWA-MEM algorithm was then used to map paired-end reads passing the pre-processing onto the human reference genome build 38 (EnsEMBL v82). Finally, variants were called according to the GATK best practice for somatic short variants (version 3.5.1), supplemented with cross-sample contamination and sequencing artifact filtering. In the process, tumor samples (tissue and CR culture) were paired with their patient-matched normal samples and variant calls were filtered against a panel of normals generated from the exome data of 24 healthy unrelated Finnish individuals sequenced in-house earlier.

Annotation for single nucleotide variants and short indels was performed using the Annovar tool against the RefGene database. In brief, variants called from samples were filtered for false-positives by removing variants not passing all GATK filters, residing in intronic and intergenic regions, and causing a synonymous or non-frameshift change as well as variant with a minor allele frequency $\geq$ 1% in the EPS, 1KG, general ExAC (ExAC), East Asian ExAC (ExAC_EAS), non-Finnish European ExAC (ExAC_NFE), Finnish ExAC (ExAC_FIN) databases, strand odd ratio for single nucleotide variants $\geq$ 3.00, and strand odd ratio for indels $\geq$ 11.00, coverage $\leq$ 10, and variant quality value $\leq$ 40. Finally, variants were removed if the variant allele frequency between the tumor and normal was < 2%. Tools used in the variant calling process and their versions have been outlined earlier.[56] Surgical samples were used to generate information for 578 cancer-related genes and data generated using this methodology is presented in Table 1.

NGS analysis of lung cancer biopsies

Upfront NGS screenings were routinely performed for all the AC and ASC patients but not for SCC patients at Helsinki University Central Hospital (HUCH) before treatment initiation or surgery. DNA was extracted from paraffin samples after pre-treatments with the Maxwell RSC (Promega), according to the manufacturer's instructions. The concentration of the DNA samples was measured using the NanoDrop ND 1000 (Thermo Fisher Scientific). Amplification-based NGS was performed to identify mutations in all exons of *PIK3CA, EGFR, KIT, KRAS, MET, NRAS,* and *PDGFRA* as well as exons 11-15 of *BRAF*-gene by using an in-house gene panel. Briefly, multiplex PCR was performed with 10 ng of genomic DNA, and then adapters were ligated to each PCR product. The amplicon libraries were constructed, and the quantity of amplicon libraries was determined using the Ion Library TaqMan Quantitation Kit (Thermo Fisher Scientific). Each library was diluted to a concentration of 10 pM, and pooled in equal volumes. Template preparation was performed with an Ion Chef Instrument, and sequencing was carried out on an Ion S5 System with PI Chip. Data was generated using the Torrent Suite Software version 5.8 (Thermo Fisher Scientific). The Ion Reporter Software version 4.6 (Thermo Fisher Scientific) was used to filter out non-coding and polymorphic variants. Mean sequencing depth $\geq$ 1000 was considered as successful sequencing and called variants were only accepted if allele frequency $\geq$ 1%. All variants listed after filtering were visualized in the Integrative Genomics Viewer (IGV) to manually discard alterations generated by incorrect calling. Core needle biopsy samples were used to generate information for 8 lung cancer-related genes and data generated using this methodology is presented in Table S1 and Figure S3.

KRAS mutation analysis

Snap-frozen cell pellets of tumor-derived EpCAM+ and EpCAM– cells were utilized to detect *KRAS* mutation variant allele frequencies using digital droplet PCR. DNA was extracted from cell pellets with the Maxwell RSC (Promega), according to the manufacturer's instructions. The concentration of the DNA samples was measured using a NanoDrop ND 1000 (Thermo Fisher Scientific). Targeted WT and mutation probes for the *KRAS* mutation sites G12 and G13 were designed according to Bio-Rad specifications (https://www.bio-rad.com). For each reaction, 2 μl of the extracted DNA was used and performed in duplicate. The QX200 Droplet Generator partitioned the samples (20 μl into 20,000 droplets) for PCR amplification. Following amplification using a thermal cycler,

droplets from each sample were analyzed individually on the QX200 Droplet Reader, where positive and negative droplets were counted to provide absolute quantification of the target DNA in digital form. The results were analyzed with the QuantaSoft Analysis Pro Software (v.1.0, Bio-Rad). Data generated for *KRAS* mutation variant allele frequencies is presented in Table S1 and Figure S3.

Statistical analyses

To assess statistical significance, a Student's t test, nonparametric Mann-Whitney test, or a two-sided Wilcoxon signed-rank test (Figure 6A) were used. The results were considered statistically significant if a p value < 0.05 was observed. Error bars indicate standard deviation or standard error of the mean. Pearson's correlation coefficients were used to assess the significance of correlations and displayed in the XY plots. All the graphs presented here, including dose-response curve fits were generated using GraphPad Prism 8 (GraphPad Software Inc). Statistical details and number of samples used for a particular result can be found in the figure legends.

Cell Reports Medicine, Volume *2*

Supplemental information

Functional diagnostics using fresh uncultured lung tumor cells to guide personalized treatments

Sarang S. Talwelkar, Mikko I. Mäyränpää, Lars Søraas, Swapnil Potdar, Jie Bao, Annabrita Hemmes, Nora Linnavirta, Jon Lømo, Jari Räsänen, Aija Knuuttila, Krister Wennerberg, and Emmy W. Verschuren

Talwelkar et al.

Supplemental Information

Table of contents:

Supplementary Figures

Figure S1

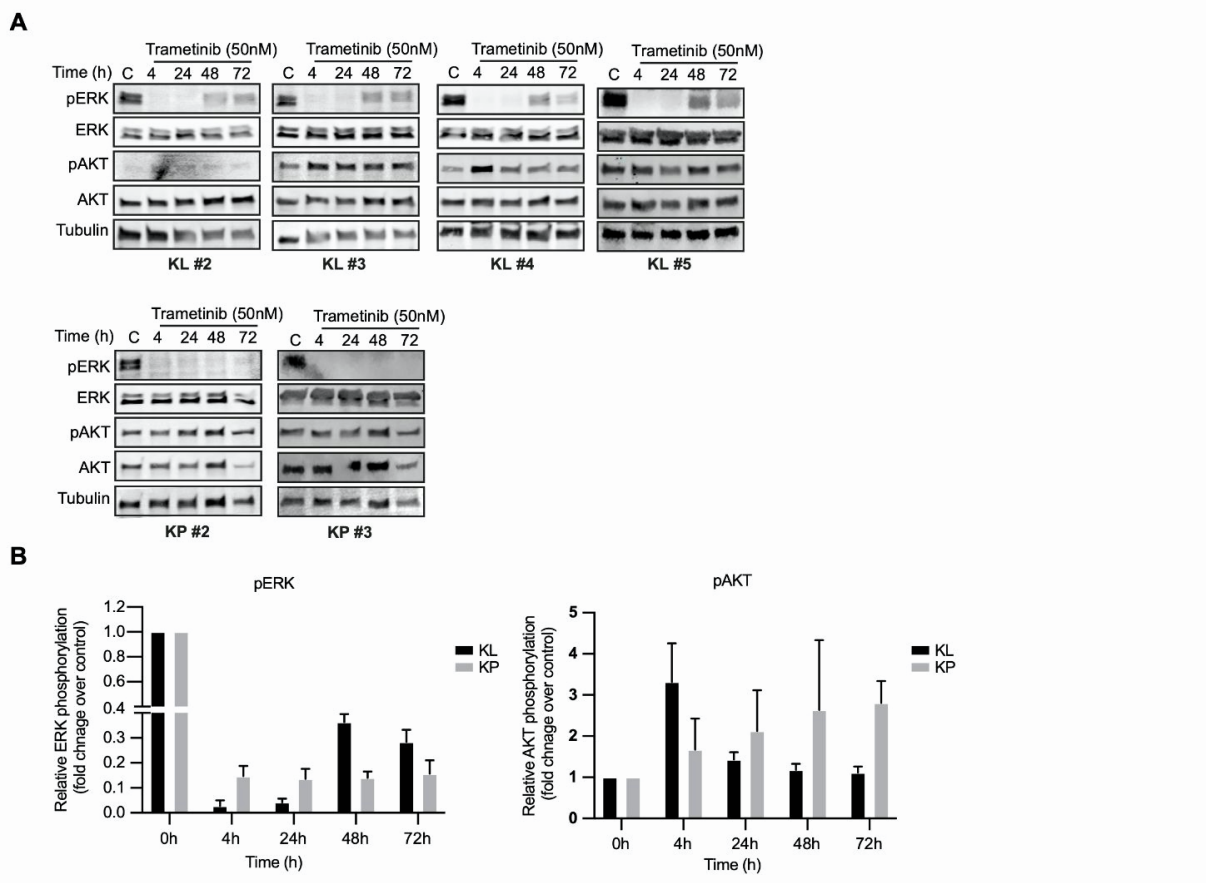

Figure S1. Analysis of trametinib-induced signaling rewiring. Related to Figure 2. (A) Immunoblots of KL and KP FUTCs treated with vehicle (C; DMSO) and or treated with 50 nM TR for various time points (4, 24, 48, and 72 h), and probed with indicated antibodies. (B) Relative quantification of pERK and pAKT signals on immunoblots presented in Figure 2D and S1A. Error bars represent ± SEM.

FIGURE S2

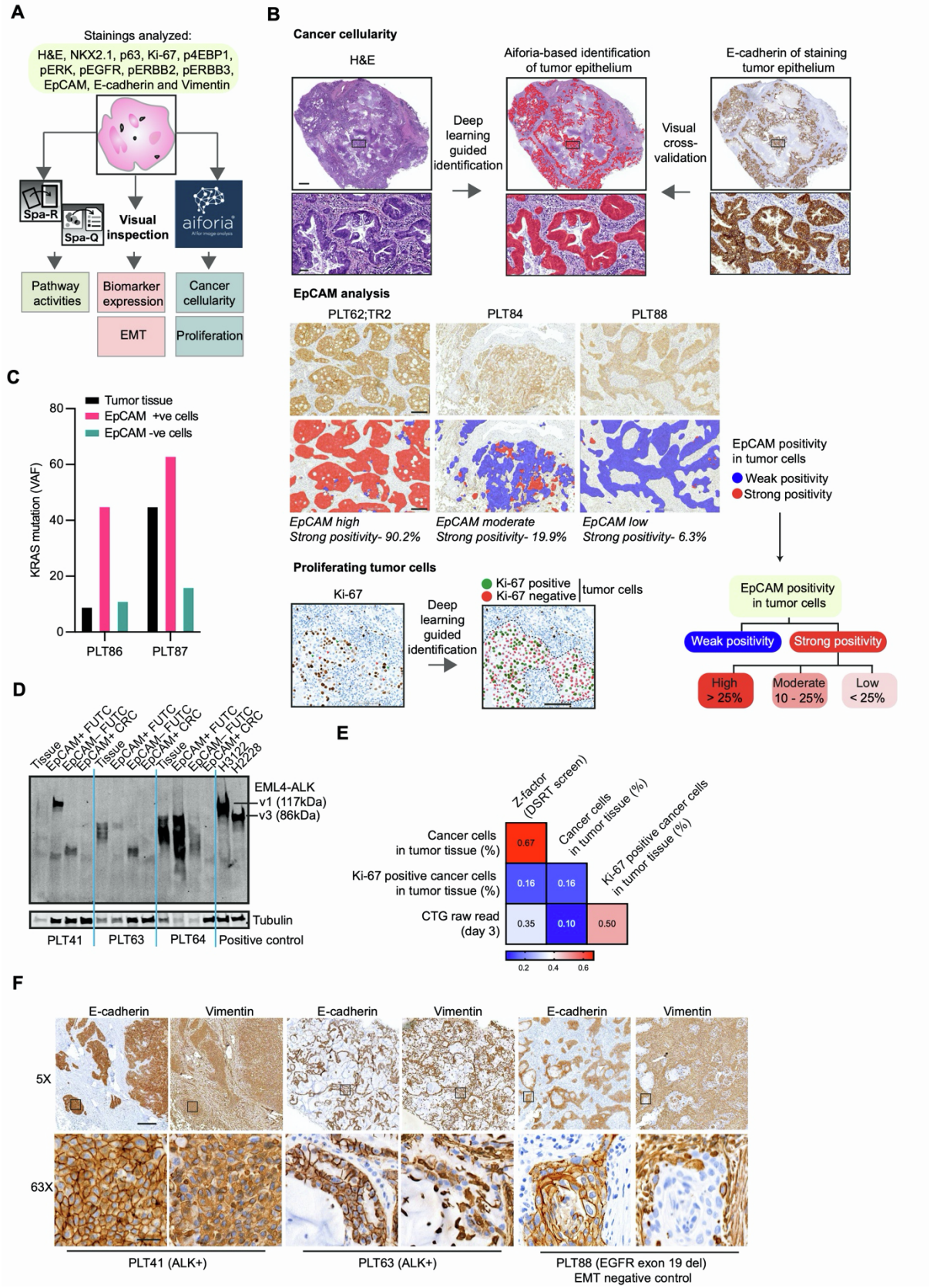

Figure S2. Tumor tissue phenotyping and biochemical analysis of clinical samples. Related to Figure 3 and 4. (A) The image analysis software package Spa-RQ[5] was used for quantification of signaling activities in tumor regions. To identify cancer cellularity, percentage of EpCAM positive cancer cells, and percentages of

Ki-67 positive proliferating cancer cells, deep learning-based Aiforia software was used. Biomarker expression and EMT status was visually assessed for each tumor sample. (B) Top panel: representative images demonstrating H&E staining (left), tumor epithelium identified using Aiforia (middle), and the validation via epithelial staining of an adjacent tissue section stained with E-cadherin (right). Scale bars correspond to 1 mm or 50 μm for low or high magnifications, respectively. Middle panel: representative EpCAM stained images and Aiforia-based detection of tumor cells exhibiting strong (red) and weak (blue) EpCAM positivity. Based on the percentage of cancer cells exhibiting strong EpCAM positivity, samples were further subclassified into high (> 25%), moderate (10 - 25%), or low (< 10%). Scale bars correspond to 200 μm. Bottom panel: representative Ki-67 stained images and Aiforia-based detection of Ki-67 positive (green) and negative (red) tumor cells. The black dotted line indicates the edge of the tumor epithelium region identified by Aiforia in a separate analysis. Scale bars correspond to 100 μm. (C) KRAS variant allele frequencies in tumor tissue and tumor-derived EpCAM+ and EpCAM– cells. (D) Immunoblot of EML4-ALK+ patient samples analyzed to verify the expression of ALK fusion protein in patient-matched tumor tissue, tumor-derived EpCAM+ and EpCAM– cells, or CR cultures (passage #4). Samples from H3122 and H2228 cells (EML4-ALK+ cell lines) were used as positive controls for v1 (117 kDa) and v3 (86 kDa) variants of EML4-ALK fusion proteins. (E) Heatmap displaying Pearson correlation coefficient values between various factors associated with FUTC-based drug testing. (F) Representative IHC images of E-cadherin and vimentin staining in patient-derived EML4-ALK+ lung tumor tissues. Scale bars correspond to 200 μm or 20 μm for low or high magnifications, respectively. Boxes indicate areas depicted at higher magnification in the bottom row.

FIGURE S3

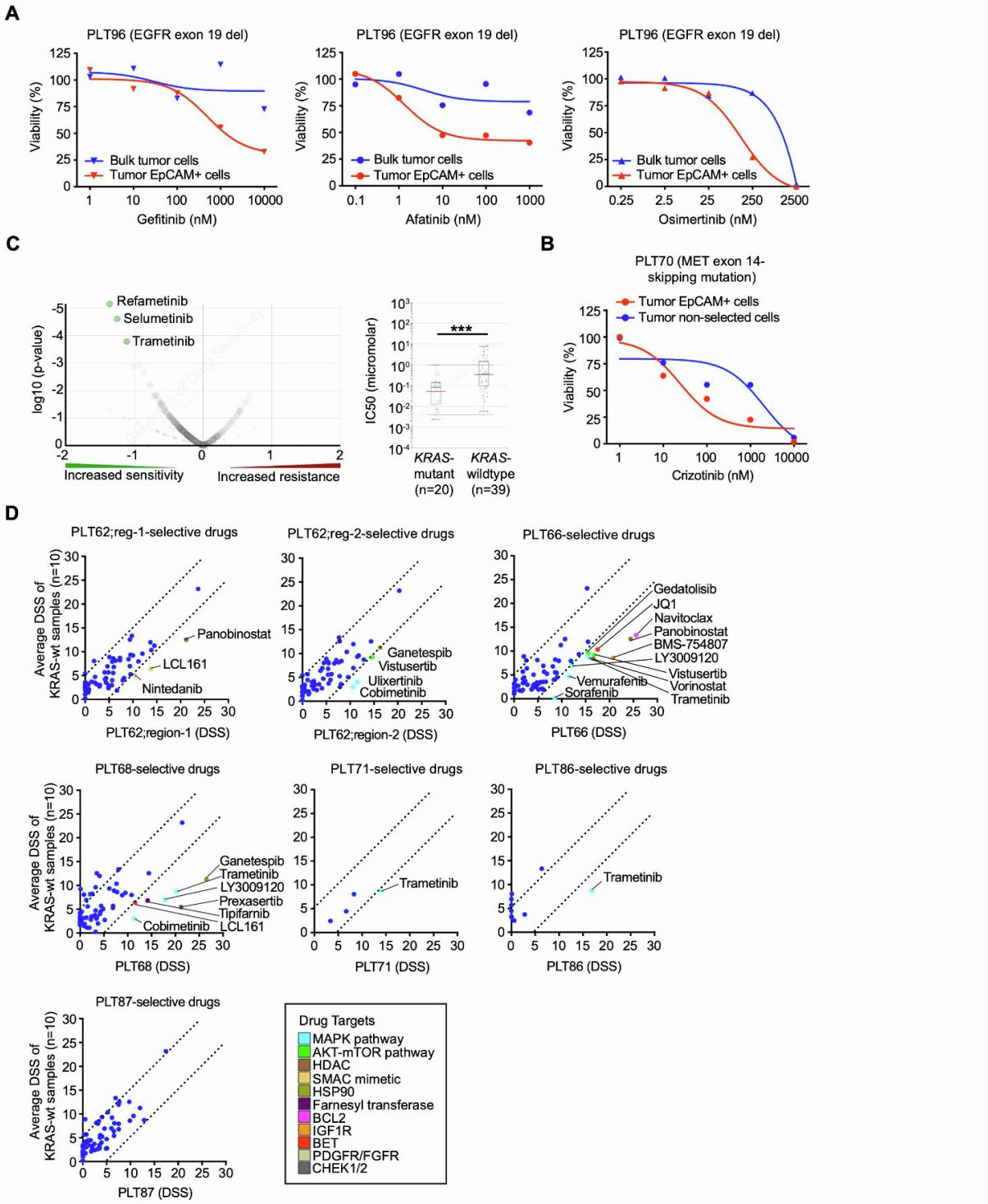

Figure S3. Drug response correlation to identify *KRAS* mutant-selective drug sensitivities. Related to Figure 4 and 5. (A) Dose-response curves of gefitinib, osimertinib, and afatinib in patient-matched tumor-derived bulk cells and EpCAM+ cells. (B) Dose-response curves of crizotinib in patient-matched tumor-derived bulk cells and EpCAM+ cells. (C) A volcano plot (left) and box plot (right) representation adapted from Genomics of Drug Sensitivity in Cancer (GDSC1) database, showing association between MEK inhibitor sensitivity and KRAS mutation in lung adenocarcinoma cells. (D) Identification of patient-selective drug vulnerabilities by comparison of DSSs of individual *KRAS* mutant samples to average DSSs of *KRAS* wildtype samples (n=10). Drugs showing *KRAS* mutant sample-selective drug sensitivities (DSS difference >5) are color coded based on their target.

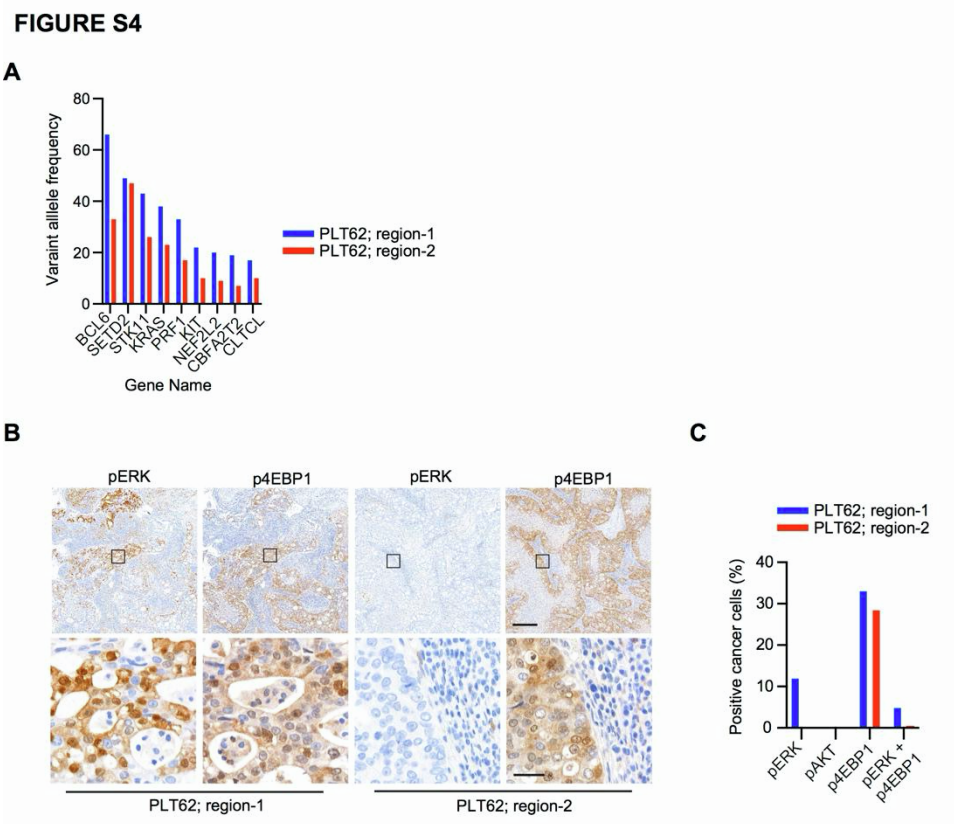

Figure S4. Analysis of intratumoral genomic and phenotypic heterogeneity in a *KRAS* mutant lung cancer specimens. Related to Figure 5. (A) Bar graph displaying the variant allele frequencies of mutations normalized to percentages of cancer cells in their respective tumor region. (B) Representative IHC images of pERK, pAKT, p4EBP1 IHC staining in different regions of the PLT62 tissue sample. Scale bars correspond to 200 μm or 20 μm for low or high magnifications, respectively. (C) Bar graph displaying levels of pERK (Thr202/Tyr204), pAKT (Ser473), p4EBP1 (Thr37/46) and overlapping phosphorylation of ERK and 4EBP1 levels in cancer cells quantified using the IHC image registration and quantification tool, Spa-RQ.

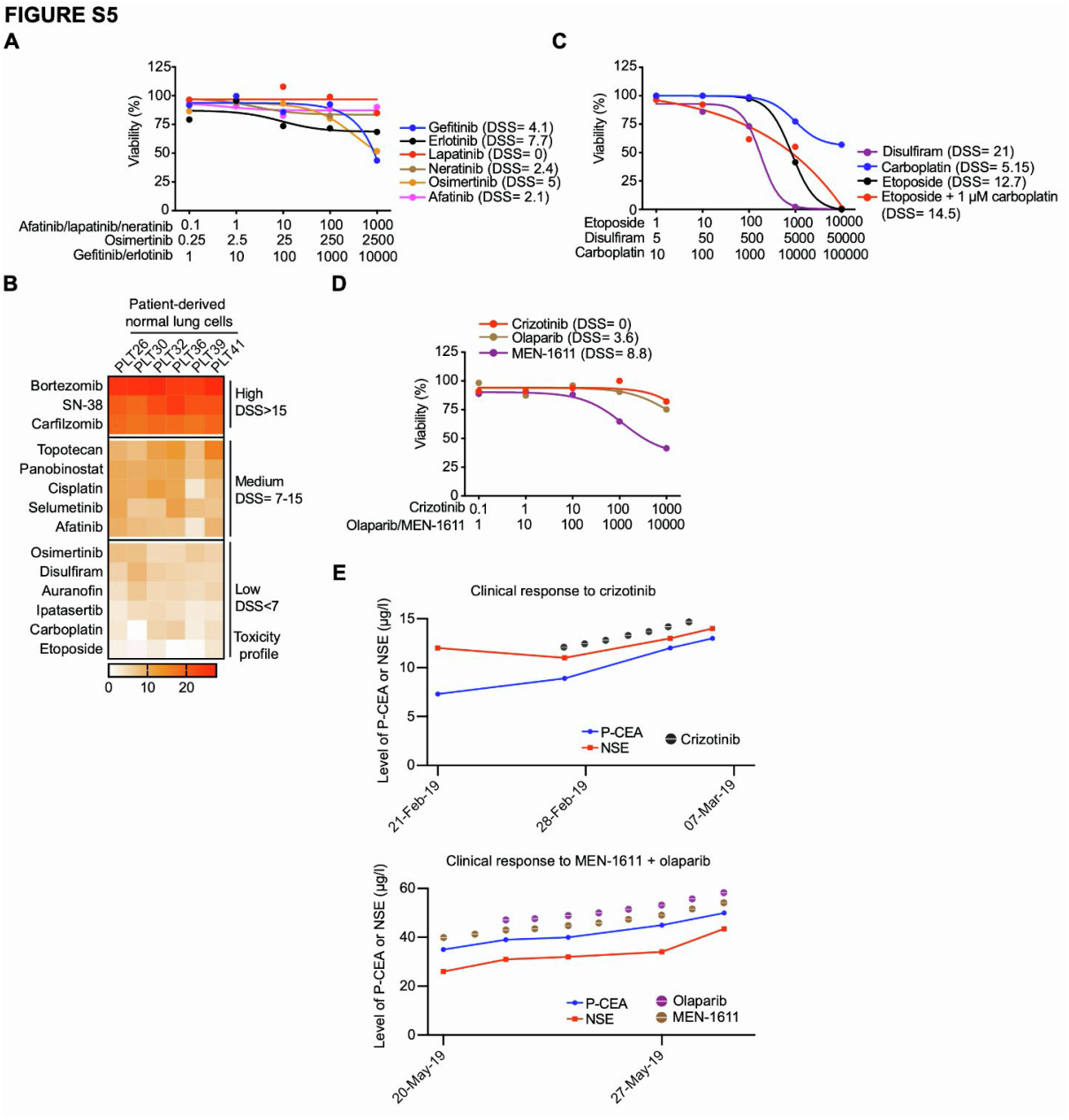

Figure S5. FUTC-based drug profiling identifies patient-selective drug sensitivities. Related to Figure 6. (A) Dose-response curves of different EGFR inhibitors in patient-derived FUTCs. (B) Toxicity profiles of top hits were assessed by testing their sensitivity in CR cultures established from healthy lung tissue of lung cancer patients. Drugs with average DSS >15 or DSS >7 are denoted as highly or mildly toxic, respectively. Drugs with average DSS <7 in the control cells were considered as putative lower toxicity compounds for clinical treatment. (C) Dose-response curves of patient-derived FUTCs treated with five doses of disulfiram, carboplatin, etoposide, and combination treatment. For the combination screen, 1 µM of carboplatin was used together with a dose series of etoposide. (D) Dose-response curves of patient-derived FUTCs treated with five doses of crizotinib, olaparib, and MEN-1611. (E) Changes in the level of CEA and NSE after treatment with crizotinib and MEN-1611 plus olaparib treatments.

FIGURE S6

A

Tumor burden before and after carboplatin plus etoposide treatment			
Body part	**Metastsis ID**	**Before treatment (11 Dec 2018)**	**After treatment (17 Jan 2019)**
Collum	Lymph node met-1	29 x 21 mm	12 x 7 mm
Collum	Lymph node met-2	12 mm	6 mm
Thorax	Lung met-1	5 x 4 mm	3 x 1
Thorax	Lung met-2	6 mm	1 mm
Thorax	Lung met-3	8 x 5 mm	4 x 3 mm
Thorax	Lung met-4	MNA	Decrease
Thorax	Lung met-5	MNA	No change
Thorax	Lung met-6	MNA	No change
Thorax	Lymph node met-3	MNA	Decreased
Thorax	Lymph node met-4	18 x 22 mm	15 x 15 mm
Thorax	Lymph node met-5	10 mm	5 mm
Thorax	Lymph node met-6	9 mm	6 mm
Abdomen/pelvis	Liver met-1	11 x 9 mm	3 x 3 mm
Abdomen/pelvis	Liver met-2	14 x 14 mm	7 x 6 mm
Abdomen/pelvis	Liver met-3	6 x 4 mm	Not found
Abdomen/pelvis	Liver met-4	10 x 7 mm	Not found
MNA: measurements not avaialable			

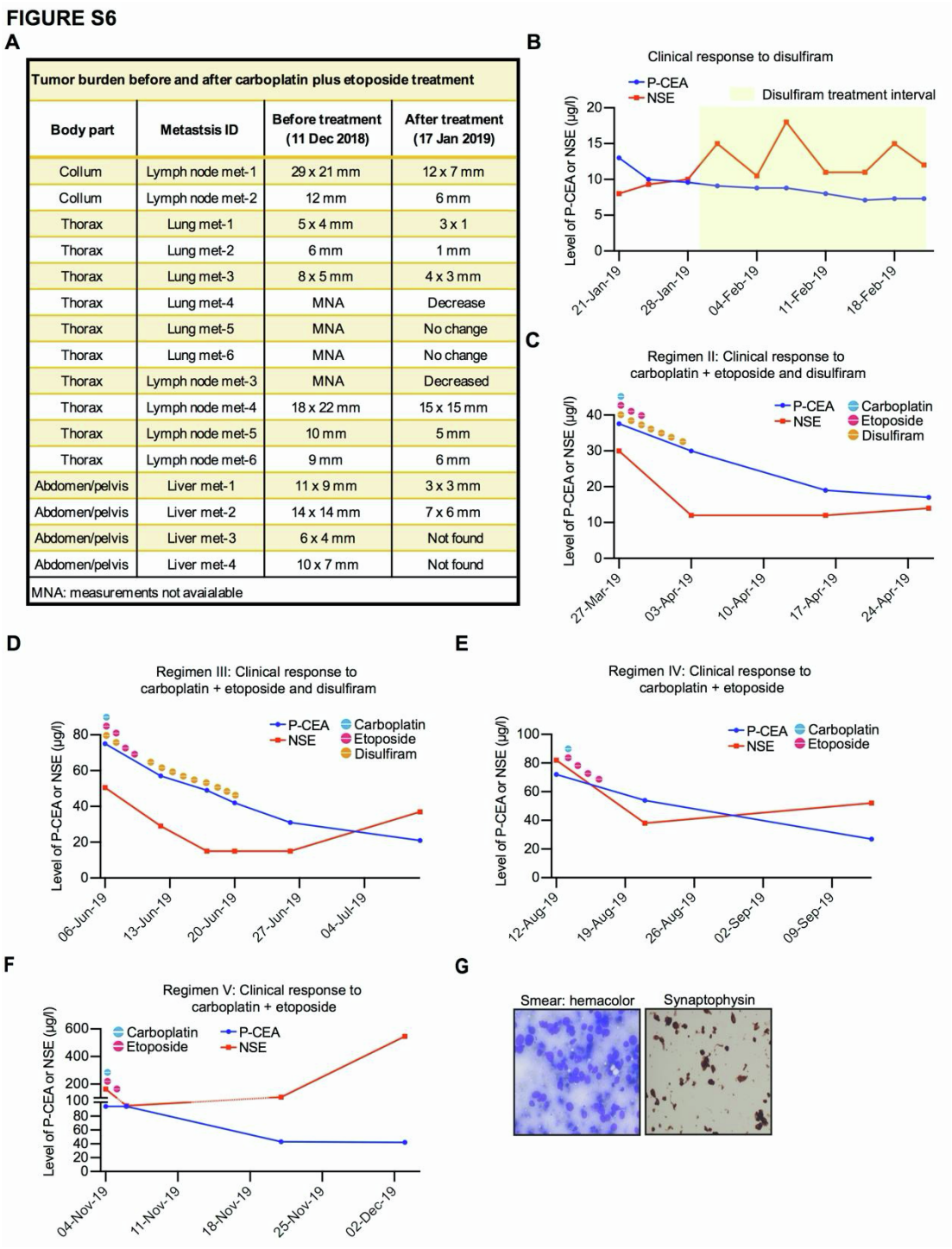

Figure S6. Clinical response to carboplatin plus etoposide treatments. Related to Figure 6. (A) Effect of disulfiram and carboplatin plus etoposide treatment on size of metastatic lesions in lymph nodes, lung, and liver. (B) Changes in the level of CEA and NSE after disulfiram treatments. (C-F) Changes in the level of CEA and NSE after carboplatin plus etoposide treatments with or without disulfiram. (G) Hemacolor stained (left) and synaptophysin (right) stains of cell smear obtained from a fine needle aspiration from a lymph node biopsy (collected in Jan 2020).

Table S1

Table S1 Clinical information of samples used for FUTC-based drug testing. Related to Figure 3.

Sample ID	Gender/age	Lung cancer	TNM stage	Oncogenic driver	Treatment	Smoking history	Tumor location
PLT37	F/73	SCC	T1bN0M0	nd	surgery	2	Left lower lobe
PLT38	M/57	AC	T3N1M0	uod	surgery	0	Left upper lobe
PLT39	M/66	MAC	results not available	uod	surgery	0	Right upper lobe
PLT41	M/56	AC	solitary recurr in mediastinum	ALK fusion +	surgery	0	Mediastinum
PLT62	F/50	AC	T2aN1M0	KRAS G13D	surgery + chemotherapy	2	Right lower lobe
PLT63	F/68	AC	T3N0M0	ALK fusion +	surgery	1	Left upper lobe
PLT64	F/25	AC	T2aN1M0	ALK fusion +	surgery + chemotherapy	0	Left lower lobe
PLT66	M/71	AC	T3N0M0	KRAS G12C	surgery	2	Right lower lobe
PLT68	F/68	AC	T1cN0M0	KRAS G12S	surgery	1	Right lower lobe
PLT70	M/82	AC	T1cN0M0	MET exon 14 skipping mutation	surgery	0	Right upper lobe
PLT71	F/58	AC	T2N0M0	KRAS G12V	surgery	2	Right lower lobe
PLT72	M/70	AC	T2bN0M0	EGFR L858R	surgery	1	Right upper lobe
PLT84	M/60	AC	T2N2M0	EGFR exon 19 del	surgery + adjuv. chemotherapy	0	Right upper lobe
PLT85	F/76	AC	T2aN0M0	EGFR L858R	surgery	0	Right upper lobe
PLT86	F/68	AC	T2N0M0	KRAS G12V	surgery + adjuv. chemotherapy	0	Right upper lobe
PLT87	F/61	AC	T3N0M0	KRAS G12C	surgery	2	Right lower lobe
PLT88	F/43	ASC	T2bN1M0	EGFR exon 19 del and EGFR amp	surgery + postop. chemoradiotherapy	0	Right upper lobe

SCC: squamous cell carcinoma, AC: adenocarcinoma, MAC: mucinous adenocarcinoma, ASC: adenosquamous carcinoma, nd: not done, uod: unknown oncogenic driver, never smoker: 0, ex-smoker: 1, current smoker: 2

Table S2

Table S2 Immunohistochemical and phenotypic characterization of clinical lung tumor tissues. Related to Figure 3, Figure 4 and Figure 5.

Sample ID	Lung cancer type	Tumor epithelial region (%)	EpCAM+ cells normalized to total cancer cells (%): strong positivity	EpCAM+ cells normalized to total cancer cells (%): weak positivity	Ki-67+ cells normalized to total cancer cells (%)	p4EBP1+ cells normalized to total cancer cells (%)	pERK+ cells normalized to total cancer cells (%)	pERK and p4EBP1 double positive cells normalized to total cancer	pEGFR positive cancer cells	pERBB2 positive cancer cells	pERBB3 positive cancer cells	E-cadherin and vimentin double positive cells
PLT37	SCC	28.15	26.35	73.65	39.82	10.25	0.00	0.00	–	–	–	–
PLT38	AC	14.3	46.85	53.15	39.32	13.58	1.47	1.03	–	–	–	–
PLT39	MAC	4.754	29.79	70.21	15.85	1.46	3.42	0.09	–	–	–	–
PLT41	AC	46.56	6.71	93.29	10.85	0.33	0.00	0.00	nd	nd	nd	+
PLT62; region1	AC	42.33	77.29	22.71	29.91	33.31	12.21	5.10	+	–	–	–
PLT62; region2	AC	49.69	90.23	7.77	32.31	28.69	0.00	0.00	+	–	–	–
PLT63	AC	21.8	18.05	81.95	9.77	9.30	5.91	0.65	–	–		+
PLT64	AC	47.3	2.795	97.205	16.26	3.51	0.00	0.00	–	–	–	+
PLT66	AC	16.68	54.6	45.4	23.71	1.19	47.56	0.47	–	–	–	–
PLT68	AC	38.07	63.61	36.39	24.69	0.09	27.13	0.01	–	–	–	–
PLT70	AC	21.14	32.53	67.47	4.28	0.30	0.00	0.00	–	–	–	–
PLT71	AC	10.84	29.43	70.57	49.58	2.47	7.17	0.18	+	–	–	–
PLT72	AC	22.51	1.67	98.33	11.11	3.46	0.00	0.88	–	–	–	+
PLT84	AC	17.73	19.97	80.03	5.82	13.85	42.23	6.32	+	+	+	+
PLT85	AC	2.574	45.09	54.01	4.39	13.96	69.05	7.79	+	+	+	–
PLT86	AC	12.99	70.57	29.43	17.45	45.18	71.58	6.46	–	–	–	–
PLT87	AC	61.15	86.99	13.01	65.42	7.44	23.24	2.41	+	+	–	–
PLT88	ASC	22.55	6.39	93.61	27.94	0.08	0.00	0.00	+	+	+	+
PLT 96	AC	12.39	30.64	69.36	10.89	nd	nd	nd	nd	nd	nd	nd

SCC: squamous cell carcinoma, AC: adenocarcinoma, MAC: mucinous adenocarcinoma, ASC: adenosquamous carcinoma, + : present, – : absent, nd: not done

158 **Table S3**

Table S3 DSS comparison between KRAS mutant cells and KRAS wildtype cells for 66 oncology drugs . Related to Figure 5.

KRAS-selective hit ID	Drug Name	Mean Diff	Median Diff	p.val	adjusted Pval	t.test	t.adjust
1	Trametinib	8.060	7.850	0.004	0.262	0.001	0.072
2	Panobinostat	4.633	1.350	0.268	0.937	0.245	0.737
3	LY3009120	4.227	2.600	0.149	0.937	0.114	0.737
4	Ganetespib	3.884	2.300	0.745	0.958	0.424	0.737
5	Cobimetinib	3.103	0.100	0.329	0.937	0.199	0.737
6	Ulixertinib	2.573	4.400	0.191	0.937	0.370	0.737
7	Sorafenib	2.083	0.000	0.353	0.937	0.280	0.737
8	Ravoxertinib	1.577	1.500	0.254	0.937	0.349	0.737
9	Olaparib	1.504	1.400	0.074	0.809	0.188	0.737
10	Gandotinib	1.366	3.000	0.415	0.937	0.376	0.737
11	Prexasertib	1.340	2.850	1.000	1.000	0.771	0.950
12	Nintedanib	1.217	1.750	0.432	0.937	0.610	0.895
13	Afatinib	1.005	5.900	0.356	0.937	0.673	0.907
14	Tipifarnib	0.996	1.150	0.745	0.958	0.652	0.906
15	LCL161	0.963	3.600	0.569	0.937	0.801	0.950
16	Vorinostat	0.821	0.700	0.876	1.000	0.761	0.950
17	Vismodegib	0.707	0.950	0.501	0.937	0.727	0.941
18	Gedatolisib	0.683	1.900	0.755	0.958	0.837	0.950
19	BMS-754807	0.669	0.050	0.935	1.000	0.848	0.950
20	JQ1	0.363	-1.300	1.000	1.000	0.914	0.955
21	Vemurafenib	0.057	-1.200	1.000	1.000	0.982	0.982
22	Dabrafenib	-0.151	0.700	0.563	0.937	0.926	0.955
23	Doxorubicin	-0.244	3.000	0.639	0.937	0.946	0.961
24	AZD4547	-0.257	0.400	1.000	1.000	0.860	0.950
25	Carboplatin	-0.297	-0.100	1.000	1.000	0.856	0.950
26	Dasatinib	-0.314	-0.050	1.000	1.000	0.896	0.955
27	Roxadustat	-0.324	-0.200	1.000	1.000	0.864	0.950
28	Vistusertib	-0.417	-2.000	1.000	1.000	0.912	0.955
29	Chloroquine	-0.500	-1.550	1.000	1.000	0.808	0.950
30	PAC-1	-0.531	-0.400	0.807	0.987	0.659	0.906
31	TAK-715	-0.796	-2.150	0.508	0.937	0.574	0.876
32	Sonidegib	-0.881	0.000	0.440	0.937	0.315	0.737
33	Perifosine	-0.884	-0.750	0.456	0.937	0.296	0.737
34	Alpelisib	-0.920	-1.200	0.394	0.937	0.391	0.737
35	Metformin	-0.923	-0.500	0.238	0.937	0.183	0.737
36	Foretinib	-1.003	-1.450	0.608	0.937	0.447	0.737
37	Docetaxel	-1.027	1.550	0.684	0.958	0.647	0.906
38	KU-60019	-1.030	-0.100	0.522	0.937	0.284	0.737
39	Volasertib	-1.126	-1.100	0.102	0.937	0.062	0.737
40	Cabozantinib	-1.130	0.600	0.934	1.000	0.416	0.737
41	Ipatasertib	-1.176	-2.600	0.755	0.958	0.704	0.929
42	Ponatinib	-1.287	-0.475	0.628	0.937	0.444	0.737
43	Palbociclib	-1.303	-1.300	0.515	0.937	0.472	0.760
44	Veliparib	-1.320	-0.700	0.463	0.937	0.264	0.737
45	Osimertinib	-1.428	-0.950	0.518	0.937	0.446	0.737
46	Dexamethasone	-1.487	0.000	0.717	0.958	0.370	0.737
47	Birabresib	-1.664	-2.000	0.639	0.937	0.584	0.876
48	Gefitinib	-1.677	1.300	0.792	0.987	0.389	0.737
49	Dovitinib	-1.711	-0.200	0.741	0.958	0.389	0.737
50	Lapatinib	-1.743	-0.100	0.066	0.809	0.250	0.737
51	NVP-LGK974	-1.813	-1.550	0.623	0.937	0.217	0.737
52	Gemcitabine	-1.888	-2.275	0.429	0.937	0.186	0.737
53	Crizotinib	-1.902	-2.700	0.136	0.937	0.069	0.737
54	Ralimetinib	-1.971	-1.550	0.515	0.937	0.255	0.737
55	VE-821	-2.069	-1.400	0.260	0.937	0.070	0.737
56	Ruxolitinib	-2.171	-1.100	0.624	0.937	0.330	0.737
57	Ceritinib	-2.492	-1.725	0.228	0.937	0.201	0.737
58	Pomalidomide	-2.869	-2.000	0.116	0.937	0.182	0.737
59	Vincristine	-2.994	-1.700	0.326	0.937	0.155	0.737
60	Azacitidine	-3.344	-3.650	0.073	0.809	0.069	0.737
61	Navitoclax	-3.365	-5.325	0.628	0.937	0.486	0.764
62	Dinaciclib	-3.503	-7.100	0.432	0.937	0.438	0.737
63	Everolimus	-3.991	-4.000	0.074	0.809	0.061	0.737
64	Pictilisib	-4.691	0.000	0.569	0.937	0.155	0.737
65	Idasanutlin	-4.938	-7.300	0.202	0.937	0.082	0.737
66	Cisplatin	-5.811	-1.300	0.074	0.809	0.117	0.737

159

References

1. Talwelkar SS, Nagaraj AS, Devlin JR, Hemmes A, Potdar S, Kiss EA, et al. Receptor Tyrosine Kinase Signaling Networks Define Sensitivity to ERBB Inhibition and Stratify Kras-Mutant Lung Cancers. Molecular cancer therapeutics. 2019;18(10):1863-74.
2. Potdar S, Ianevski A, Mpindi JP, Bychkov D, Fiere C, Ianevski P, et al. Breeze: an integrated quality control and data analysis application for high-throughput drug screening. Bioinformatics. 2020.
3. Yadav B, Pemovska T, Szwajda A, Kulesskiy E, Kontro M, Karjalainen R, et al. Quantitative scoring of differential drug sensitivity for individually optimized anticancer therapies. Sci Rep. 2014;4:5193.
4. Dufva O, Kankainen M, Kelkka T, Sekiguchi N, Awad SA, Eldfors S, et al. Aggressive natural killer-cell leukemia mutational landscape and drug profiling highlight JAK-STAT signaling as therapeutic target. Nat Commun. 2018;9(1):1567.
5. Bao J, Walliander M, Kovacs F, Nagaraj AS, Hemmes A, Sarhadi VK, et al. Spa-RQ: an Image Analysis Tool to Visualise and Quantify Spatial Phenotypes Applied to Non-Small Cell Lung Cancer. Sci Rep. 2019;9(1):17613.